https://doi.org/10.5194/egusphere-2026-6670
Preprint. Discussion started: 4 November 2026
© Author(s) 2026. CC BY 4.0 License.

Drivers of convection initiation in the Tropical Andes

Diego Urdiales-Flores[1], Francina Dominguez[2], Divyansh Chug[3], Grégoire Mariéthoz[1,4], Charles Jones[5], Leila M.V. Carvalho[5], and Nadav Peleg[1,4]

[1]Institute of Earth Surface Dynamics, University of Lausanne, Lausanne, Switzerland
[2]Department of Climate, Meteorology, and Atmospheric Sciences, University of Illinois Urbana-Champaign, Urbana, IL, USA
[3]Aon Impact Forecasting
[4]Expertise Center for Climate Extremes, University of Lausanne, Lausanne, Switzerland
[5]Department of Geography, University of California, Santa Barbara, CA, USA

Correspondence: Diego Urdiales-Flores (diego.urdialesflores@unil.ch)

Abstract. Severe convective events are among the leading causes of weather-related damages in the Tropical Andes. Such events, often spanning thousands of square kilometers, are governed by a combination of local and synoptic-scale processes that together create favorable conditions for atmospheric convection. Understanding these processes and conditions is essential for improving forecasting of convection initiation, impact assessment, and risk management. Here, we investigated the regional atmospheric and land surface conditions associated with convective events using remote sensing, climate reanalysis, and environmental variables. We considered local land surface characteristics (e.g., vegetation, land surface temperature, and topography), together with background atmospheric conditions, including wind speed and direction, atmospheric instability, and the occurrence of low-level jets (LLJs) in the eastern Tropical Andes, where multiple severe convective events may occur within a single day. We analyzed the atmospheric conditions preceding 111,239 convective initiation (CI) events identified from infrared satellite imagery. We found that CI occurs most frequently between September and May, peaks in the early afternoon, and that roughly three-quarters of CI events (72%) were associated with LLJs. Topographic gradients are strongly associated with CI in the high and low Andes. Vegetation and CAPE show no significant link with CI occurrence. CI tends to develop over warm surface anomalies with cooler conditions downwind, and near-surface flow dominated by NW, N, NE, and E winds. Once convection initiates, the subsequent precipitation peaks roughly 4–6 hours after CI and is strongly modulated by low-level wind direction and the presence of LLJs. Events associated with the Central and Andes Jets, when near-surface winds are predominantly from the N, NE, and E, produce nearly 3 times more precipitation than cases with NW flow or no LLJ. Interestingly, this enhanced precipitation tends to be more long-lived and moderate in intensity, rather than occurring in brief, extreme bursts. These findings highlight the importance of land–atmosphere interactions and regional atmospheric dynamics for severe convection in tropical–temperate transition regions, with direct implications for improving weather forecasting.

https://doi.org/10.5194/egusphere-2026-6670
Preprint. Discussion started: 4 November 2026
© Author(s) 2026. CC BY 4.0 License.

1 Introduction

Convective rainfall is among the most intense forms of precipitation, often producing short-duration, high-intensity events that organize over large spatial scales and trigger severe hydrometeorological hazards (Fowler et al., 2021). In mountainous tropical regions, the presence of complex topography, high moisture availability, strong surface heating, and atmospheric instability frequently leads to heavy convective precipitation and creates hotspots of intense rainfall (Urdiales-Flores et al., 2026; Benoit et al., 2024; Liu et al., 2026), posing major challenges for forecasting and risk management (Urdiales-Flores et al., 2025; Pepin et al., 2022). Moreover, understanding rainfall dynamics in complex mountainous regions is particularly important in the context of climate change (Viviroli et al., 2007), given projections indicating an increase in the frequency and intensity of localized extreme rainfall events (Peleg et al., 2025).

In tropical high-mountain regions such as the Andes, cloud and precipitation formation result from complex interactions among atmospheric processes operating across multiple spatial and temporal scales (Bendix et al., 2009; Kirshbaum and Durran, 2004). At the continental to synoptic scale, low-level jets (LLJs) regulate the large-scale transport of moisture toward and along the Andes, including its north–south redistribution (Jones et al., 2023), while mesoscale convective systems (MCSs) and mesoscale convective complexes (MCCs) organize deep convection and can generate extreme precipitation, particularly along the eastern slopes of the Andes (Rasmussen and Houze Jr, 2016; Lin, 2005; Houze Jr, 2004; Jones et al., 2023; Robledo et al., 2024). Together, these processes influence moisture supply, low-level convergence, and atmospheric conditions that govern the initiation, organization, timing, and intensity of convective precipitation.

Despite advances in understanding the atmospheric controls on severe precipitation, the mechanisms driving convection initiation (CI) and modulating tropical mountain convection remain poorly constrained. Studies in subtropical and midlatitude regions have shown that local land surface temperature gradients can influence CI by modifying surface heat fluxes and mesoscale circulations (Chug et al., 2023; Taylor et al., 2012). However, the interplay between local factors (e.g., land surface heterogeneity, vegetation, and atmospheric instability) and large-scale atmospheric features, particularly LLJs, in controlling orographic precipitation processes remains largely unexplored in the Tropical Andes (Pielke et al., 2011; Dominguez et al., 2024). This limited understanding of the coupled influences of local and large-scale controls poses a major challenge for accurately representing CI and precipitation development in tropical high-mountain environments in both observational datasets and numerical models.

Numerous studies across diverse geographic contexts demonstrate the importance of thermodynamic conditions for CI. Thermodynamic instability, commonly quantified by Convective Available Potential Energy (CAPE), provides the buoyant energy required for parcel ascent and has been identified as an important control on CI in midlatitude plains and tropical lowlands (Chen et al., 2020). However, sufficient instability alone does not guarantee CI, as additional surface and dynamical processes are required to initiate and sustain convective development (Bennett et al., 2006; Houze Jr, 2012).

Beyond these atmospheric controls, antecedent land surface conditions can further influence the likelihood of CI. Vegetation density can modify surface energy partitioning, boundary-layer development, and moisture recycling in the Andes (Bedoya-Soto and Poveda, 2024), while soil-moisture conditions have been shown to affect the development and organization of con-

https://doi.org/10.5194/egusphere-2026-6670
Preprint. Discussion started: 4 November 2026
© Author(s) 2026. CC BY 4.0 License.

vective systems in South America and North Africa (Paccini and Schiro, 2025; Petrova et al., 2018). These surface processes can also interact with atmospheric dynamics to modify local moisture availability and convective potential.

Understanding the combined influence of these thermodynamic, surface, and dynamical controls is particularly important in the Tropical Andes, where strong elevation gradients and complex terrain interact with large-scale atmospheric circulation. Improving our understanding of these processes contributes to broader efforts to advance observational and modelling capabilities in mountain environments, including international initiatives such as Multi-scale transport and exchange processes in the atmosphere over mountains – programme and experiment (TEAMx), as described by Serafin et al. (2020) and Rotach et al. (2022), which investigates exchange processes in the atmosphere over mountains at multiple scales and advances the parameterizations of these processes in numerical models for weather and climate prediction. Although TEAMx focuses primarily on European mountain ranges, the Tropical Andes provide an important tropical, high-elevation counterpart, contributing to the broader research priorities of the Mountain Research Initiative (MRI), which promotes interdisciplinary research on atmospheric processes and climate-related challenges in mountain regions (Thornton et al., 2021; Pepin et al., 2015).

Tropical easterly winds and low-level jets transport moisture from the tropical Atlantic across the Amazon basin toward the eastern Andes, accounting for roughly 60–80% of the annual climatological moisture supply over tropical South America (Jiménez-Sánchez et al., 2019, 2020; Mu et al., 2025). However, the variability of moisture transport during CI events and its contribution to their development is not well characterized. Characterizing these moisture transport patterns is therefore essential for determining whether CI development results from an enhancement of the climatological moisture inflow or from distinct moisture transport pathways.

To better understand the processes governing CI and its subsequent evolution over the Tropical Andes, we address the following research question: what local-to-regional atmospheric and land-surface conditions are associated with CI? In a second step, we explore the characteristics associated with convective precipitation, such as intensity and duration, and ask how these characteristics are related to the environmental conditions associated with CI. We analyze satellite observations and climate reanalysis datasets over the Andes of Ecuador and southern Colombia, with a focus on CI events and their surrounding environmental conditions. We characterize local-to-regional atmospheric controls (wind, CAPE, and CIN) and land-surface controls (topography, vegetation, and soil moisture) associated with CI, together with large-scale moisture transport associated with LLJs. These environmental conditions are characterized during the period preceding CI, while precipitation properties are analyzed following CI occurrence. Composite analyses and statistical correlation methods are employed to investigate the relationships among land–atmosphere interactions, precipitation characteristics, and large-scale atmospheric dynamics associated with CI and its subsequent evolution.

2 Study region

The study focuses on the Andes of Ecuador and southern Colombia (5°S-5°N, 82°W-70°W), a region characterized by a predominantly tropical climate with strong elevation-driven gradients and encompassing four major eco-regions (Fig. 1a): the North Amazon basin (NAMZ), the low Andes (ANDES-L; 1000-2000 m a.s.l.), the high Andes (ANDES-H; >2000 m

https://doi.org/10.5194/egusphere-2026-6670
Preprint. Discussion started: 4 November 2026
© Author(s) 2026. CC BY 4.0 License.

a.s.l.), and the coastal plains (COAST). The Andean cordillera extends from north to south across the domain, generating steep elevation gradients (from 300 m to 4500 m, over 150-200 km distance) that give rise to diverse microclimates and pronounced spatial variability in precipitation.

The regional precipitation regime is sustained by the interaction of regional moisture transport and large-scale atmospheric circulation with local land surface and atmospheric conditions. Tropical easterly winds and low-level jets (LLJs; see Supplementary Fig. S1) supply most of South America's moisture; it remains unclear whether CI events depend on this baseline inflow or entirely distinct transport pathways. As these humid air masses approach the Andean barrier, forced ascent enhances condensation and precipitation, particularly along the eastern slopes (Staal et al., 2018; Fassoni-Andrade et al., 2021). These regional processes are further modulated by variability across seasonal to interannual timescales. Seasonal variability is driven by the migration of the Intertropical Convergence Zone (ITCZ), the evolution of the South American Monsoon System (SAMS), and the South Atlantic Convergence Zone (SACZ). Interannual variability is primarily associated with the El Niño-Southern Oscillation (ENSO), which influences not only precipitation patterns but also atmospheric circulation and temperature trends (Imfeld et al., 2021; Urdiales et al., 2018). Together, these processes affect the timing, intensity, and spatial distribution of rainfall across the study area (Bendix, 2000; Bendix et al., 2006).

Convective rainfall is frequent, particularly during the afternoon, and often reaches high intensities capable of triggering flash floods and landslides in mountainous terrain (Urdiales-Flores et al., 2025; Urgilés et al., 2024). A bimodal precipitation regime presents rainfall peaks in January to May and September to December, and a pronounced dry season in June to August, with some anomalies in October due to the intensification of the easterlies and the South American Monsoon System (SAMS), producing enhanced orographic precipitation (Poveda et al., 2005; Célleri et al., 2007).

Organized convective systems can also produce widespread precipitation over the Andean foothills and inter-Andean valleys, highlighting the importance of convection in the regional hydroclimate. Consistent with these characteristics, satellite-based NASA observations (GPM-IMERG, 2023) and the multisource RAINF4PE precipitation dataset (Fernandez-Palomino et al., 2022) identify a pronounced precipitation hotspot (approximately 16-20 mm day^{-1}) along the transition between the NAMZ and the ANDES-L (Fig. 1b,c).

Regional low-level atmospheric circulation in northwestern South America is modulated by key low-level jets (LLJs; see Supplementary Fig. S1): the Choco LLJ, a west-to-east Pacific cross-equatorial flow that enters northwestern Colombia; the Northern LLJ (Orinoco LLJ), which originates in the northern Orinoco basin and feeds into the Andes LLJ, channeling moisture southward along the eastern slopes of the mountain range; and the Central LLJ. In addition, LLJs variability exhibits a strong relationship with the ENSO (Mu et al., 2024). However, ENSO is not the only coupled mode important in modulating climate in South America. The Atlantic also plays a crucial role in the summer monsoon, the cross-hemispheric flow transporting moisture inland across the Amazon Basin and Tropical Andes before turning southward (Espinoza et al., 2020). The spatial configuration, intensity, and latitudinal displacement of these core circulation pathways are closely linked to the seasonal migration of the ITCZ.

https://doi.org/10.5194/egusphere-2026-6670
Preprint. Discussion started: 4 November 2026
© Author(s) 2026. CC BY 4.0 License.

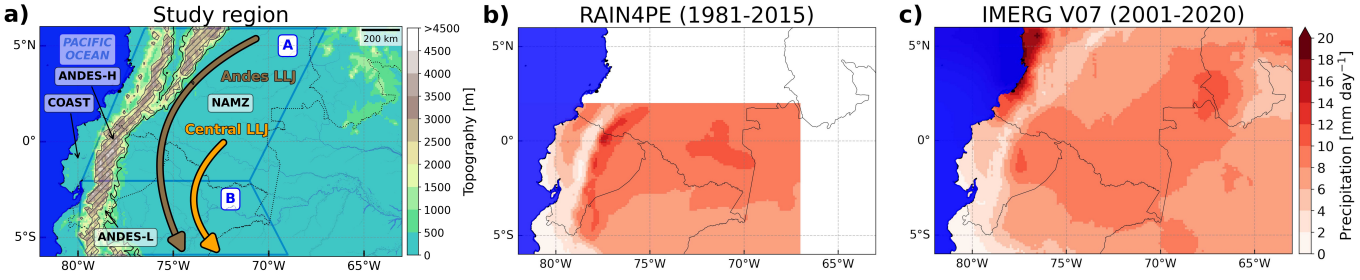


Figure 1. (a) Topography of the study area and partition to eco-regions (following Urdiales-Flores et al., 2025): North Amazon basin (NAMZ), Andes high mountains (ANDES-H), Andes low mountains (ANDES-L), and coastal plains (COAST). Blue polygons denote regions A and B, corresponding to areas influenced by low-level jets (LLJs), as described in Section 4.4. (b) Annual mean daily precipitation based on RAINF4PE dataset during 1981-2015. (c) Same as (b) but using Integrated Multi-satellitE (IMERG) V07 during 2001-2020.

3 Conceptual framework

The development of convective rainfall generally requires sufficient atmospheric moisture, an unstable atmospheric profile, and a lifting mechanism capable of initiating local updrafts (Bendix et al., 2009). Following CI, clouds can develop rapidly in the vertical direction, evolve and propagate, produce precipitation, and eventually dissipate. This life cycle typically occurs over spatial scales of 10-100 km and temporal scales of 30-180 min, as illustrated in Fig. 2 and described by Gupta et al. (2024) and Prein et al. (2023).

The methodological framework used to detect CI, characterize its associated land surface and atmospheric conditions, and track the subsequent precipitation is summarized schematically in Fig. 2: (A) we identified the locations and times of CI events using satellite infrared observations; (B) we then assessed other local atmospheric variables, including conditions associated with lifting and convective instability; (C) using the detected CI events, we then examined whether CI preferentially occurred in association with particular antecedent land surface temperature patterns, which were used as a proxy for spatial variations in soil moisture; (D) and characterized the large-scale atmospheric and synoptic conditions, including the occurrence of low-level jets (LLJs); (E) finally, we tracked the precipitation following CI in space and time and analyzed its properties. The specific methods applied at each stage are described in the following subsections.

https://doi.org/10.5194/egusphere-2026-6670
Preprint. Discussion started: 4 November 2026
© Author(s) 2026. CC BY 4.0 License.

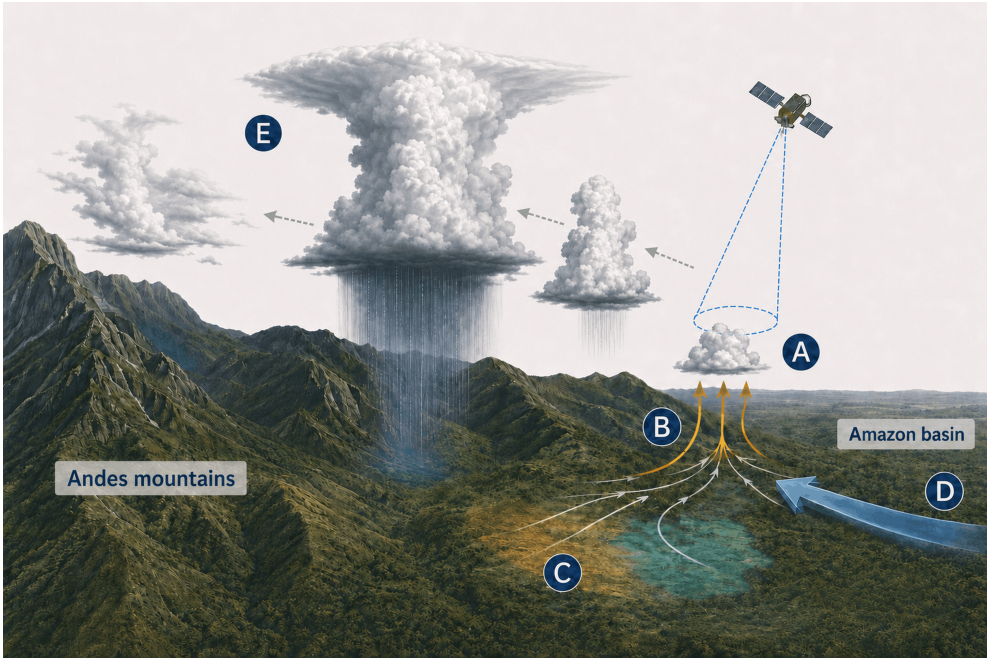


Figure 2. Schematic illustration of convective rainfall development and the methods employed to characterize local and large-scale atmospheric drivers of convection initiation events in the Tropical Andes and their precipitation properties. A) Tracking nascent-stage convective features (i.e., CI; Section 4.1); B) Analyzing lifting, local atmospheric and land surface controls on Convection Initiation (Section 4.2); C) Analyzing land surface temperature anomalies (Section 4.3) ; D) Analyzing large-scale circulation and low-level jets (LLJs) (Section 4.4); E) Analyzing precipitation properties after convective onset (Section 4.5). Adapted from Fig. S2 using ChatGPT for assistance. For more detail on inputs, processing, and outputs, see Supplementary Fig. S3.

4 Methods and data

4.1 Tracking nascent-stage convective features

We started by identifying the locations and times of the initial development of deep convective clouds. These clouds are detected using infrared satellite imagery from NASA (GPM-MERGIR (2023)), where local minima in brightness temperature are commonly associated with the presence of deep convection. We employed a globally merged infrared brightness temperature dataset (Tb, equivalent blackbody temperature) at 4 km spatial and 30 min temporal resolution, derived from observations collected by multiple geostationary satellites (Janowiak et al., 2005), corrected for zenith angle dependence to reduce the cold bias at locations far from satellite nadir.

We followed the methodology initially introduced by Barton et al. (2021) and further refined by Chug et al. (2023), which comprises the following criteria:

https://doi.org/10.5194/egusphere-2026-6670
Preprint. Discussion started: 4 November 2026
© Author(s) 2026. CC BY 4.0 License.

1. **Initial-stage deep convective cloud detection.** Deep convective clouds are identified during their initial growth stage by restricting detections to areas no larger than 20 km x 20 km. At the 4-km satellite Tb resolution, this area corresponds to a 5 x 5 pixel region, hereafter referred to as a "cloud window". Candidate cloud windows are identified by scanning the Tb field for 5 x 5 regions whose minimum brightness temperature occurs at the central pixel, indicating a cold-core structure. A cloud window is classified as deep convective when this central minimum temperature is below 235 K.

2. **Cloud window isolation and cooling-rate selection.** To minimize contamination from preexisting or propagating clouds, detected systems are required to be newly developing and undergoing rapid cooling. We imposed a cloud-free condition within a 12-km radius around the cloud window, where all surrounding pixels must have Tb values warmer than 253 K (Mapes and Houze Jr, 1993). The temporal evolution of the minimum Tb within the cloud window and its surrounding area was then evaluated. A linear regression was applied to the minimum Tb values over the previous hour using two earlier time steps (spanning two preceding 30-min time steps), and the resulting cooling rate (K h^{-1}) must exceed a threshold corresponding to rapid cooling, defined as a slope of less than -10 K h^{-1}. A sensitivity analysis of the parameters is presented in Supplementary Fig. S4, demonstrating that the selected parameters are appropriate for identifying nascent-stage convective features in the region.

3. **Parallax correction.** The geolocation of tracked cloud features is affected by the parallax induced by their finite cloud-top height because the satellite observes clouds from an oblique viewing geometry; the apparent position of a cloud in the satellite image can be displaced relative to its actual location at the Earth's surface. Correcting this displacement therefore requires an estimate of cloud-top altitude. We estimated cloud-top heights by vertically matching the hourly satellite-derived cloud-top temperatures to monthly mean atmospheric temperature profiles from ERA5 (Hersbach et al., 2020). The corresponding pressure levels were converted into altitude using the associated geopotential height fields, following the well-known Vicente et al./Koenig algorithm (Bieliński, 2020). ERA5 was not used to provide fine-scale spatial geolocation, but rather as a physically consistent atmospheric background for estimating the cloud-top height required for the parallax correction. A time-invariant monthly atmospheric background was assumed throughout each month.

4. **Water body proximity filtering.** To minimize the influence of convection linked to surface water features, CI events occurring within a 10-km radius of water bodies exceeding 10 km^2 were removed using the MOD44W (version 6, 2015 data) land–water mask (Carroll et al., 2017) (Fig. 1a).

Upon fulfillment of all detection criteria, the center location of the identified cloud window was recorded as the CI occurrence, together with its corresponding detection time. The detection algorithm was systematically applied to all 5 x 5 cloud windows across the study domain during daytime, and CI events are defined as those occurring between 6:00 and 18:00 local time to isolate mechanisms associated with diurnal thermal convection throughout the year over tropical region for the period 2001–2020, corresponding to the joint availability of all required satellite observations and reanalysis datasets. Given the proximity of the study region to the equator, CI events detected shortly after 06:00 local time may also reflect nocturnal convection

https://doi.org/10.5194/egusphere-2026-6670
Preprint. Discussion started: 4 November 2026
© Author(s) 2026. CC BY 4.0 License.

and associated outflow boundaries or low-level jets, rather than solely daytime thermal forcing. Nevertheless, this potential contribution does not compromise the consistency of the CI detection framework or the comparability of events across the study period. We then computed the following:

(i) Initiation density. CI were aggregated onto a 0.25° x 0.25° spatial grid to characterize their spatial distribution. The CI density was calculated at each grid cell as the number of detected CI events normalized by the grid-cell area and the total number of analyzed days;

(ii) Diurnal probability distribution. The diurnal probability distribution of tracked CI events was derived by aggregating event initiation times by UTC hour. The number of CI events initiated within each hourly interval was normalized by the total number of tracked CI events;

and **(iii) Distribution of CI event durations.** To characterize the temporal persistence of detected CI events, the duration of each event was calculated as the elapsed time between its first identification and its termination according to the CI tracking procedure. The resulting event durations were then aggregated to construct probability distributions, allowing the assessment of the frequency and variability of CI lifetimes.

4.2 Local atmospheric and land surface controls on Convection Initiation (CI)

We next examined the relationships between land surface (topography, vegetation greenness) and atmospheric (wind, CAPE, CIN). These parameters were selected as they represent the primary surface, dynamic, and thermodynamic drivers of convective triggering. Specifically, CAPE and CIN reflect the buoyant energy and convective inhibition governing parcel ascent, vegetation greenness modulates surface energy partitioning and boundary-layer moisture, and topography along with wind speed and direction dictates local moisture convergence and terrain-induced mechanical lifting. Although ERA5 CAPE and CIN are coarse relative to local topographic variability, they represent the broader-scale thermodynamic environment in which convection develops and therefore provide a useful background for assessing its relationship with locally resolved topography. Wind direction and speed were obtained at the CI location from hourly ERA5 10-m wind vectors and averaged over the 2 h preceding initiation (Yoon et al., 2026), following the approach described in Section 4.3 for the MODIS land surface temperature (LST). Based on these estimates, we computed: **(i)** the percentage of CI events by wind direction, **(ii)** the distribution of CI cases according to mean wind direction, **(iii)** the seasonal distribution of CI cases by wind direction, and **(iv)** the distribution of wind speed of CI cases by wind direction. To ensure statistical robustness and avoid artifacts from infrequent directional sectors, wind categories representing less than 10% of total CI events were excluded from further examination of driver relationships.

The Global Multi-resolution Terrain Elevation Data 2010 (GMTED, 2010) at 30-arc-second spatial resolution was used to extract topographic cross-sections extending 100 km upwind and downwind of each CI location. These elevation profiles allow us to quantify how local terrain features trigger convection through mechanical orographic lifting and flow convergence along the low-level wind vector.

Monthly mean enhanced vegetation index (EVI) from the MODIS/Terra (MOD13C2) (2023) version 6 product (0.05° spatial resolution) (Didan, 2015) was used to characterize vegetation conditions associated with each CI event. EVI anomalies

https://doi.org/10.5194/egusphere-2026-6670
Preprint. Discussion started: 4 November 2026
© Author(s) 2026. CC BY 4.0 License.

were calculated as the difference between the EVI value at the time of the CI event and the corresponding regional monthly mean EVI (Fig. 6b). The EVI corresponding to the time of CI initiation was also analyzed.

Hourly ERA5 convective available potential energy ($CAPE$) and convective inhibition (CIN) estimates were extracted at the CI location and averaged over the 2 h before initiation. This procedure is analogous to the LST approach (Section 4.3), but using $CAPE$ and CIN variables.

4.3 Mean land surface temperature anomalies

Spatial variations in soil moisture (SM) can contribute to CI by modifying the partitioning of surface energy between sensible and latent heat fluxes, which can result in contrasts in near-surface temperature and humidity that can generate local convergence and uplift, thereby creating conditions favourable for CI (Petrova et al., 2018; Paccini and Schiro, 2025). To examine this relationship, we characterized antecedent conditions for detected daytime CI events using daily MODIS land surface temperature (LST) and emissivity data (MODIS/Terra (MOD11C1), 2021), treating temperature anomalies as a proxy for spatial variations in SM and associated surface-flux contrasts (Chug et al., 2023).

Daily morning LST observations (K), acquired at approximately 0830 LT from the level-3 MODIS/Terra dataset (version 6.1), were used throughout the study period (2001–2020). The data are provided at a spatial resolution of 0.05° ($\sim$ 5.6 km at the equator) (Wan et al., 2021). MODIS LST is obtained from thermal infrared measurements (3.66-12.27 μm) using atmospheric corrections and clear-sky retrievals. Only land pixels with a confidence level of $\geq 95\%$ are included, ensuring cloud-free LST estimates. Remaining cloud effects would bias temperatures low and weaken the detected LST gradients.

Once LST were obtained, a composite of mean surface LST conditions across all CI events was computed. For each CI event, two-dimensional surface anomaly transects were aligned with the direction of the background wind. The background wind was derived from hourly 10-m ERA5 wind fields (Hersbach et al., 2020), spatially averaged within a $1^\circ \times 1^\circ$ domain centered on the CI location and temporally averaged over the 2 h preceding the initiation time, representing the pre-storm atmospheric state immediately before convective initiation (Yoon et al., 2026). Composite mean land surface temperature anomalies (LSTA) are then obtained by averaging the rotated transects across all CI events.

In addition, we calculated CI-centred LSTA gradients along the downwind direction to test whether CI preferentially occurred in association with surface-temperature contrasts that could promote local convergence and uplift. Initiation gradients were calculated as the slope of the linear regression between LSTAs and distance from the CI location to a downwind point at L km, where L defines the surface heterogeneity length scales. To evaluate whether these gradients were distinct from background LSTAs, up to eight noninitiation gradients were sampled near the edges of the rotated two-dimensional transects for each CI event. The significance of the mean initiation gradient was evaluated using a bootstrap approach (Wilks, 2011) by comparing it with a distribution derived from a combined set of initiation and noninitiation gradients. For a sample of N initiation gradients, 1000 bootstrap realizations were generated by randomly selecting N gradients with replacement from this combined dataset. The observed mean initiation gradient was considered significant when it fell not within the corresponding confidence limits of the bootstrap distribution. The noninitiation gradients provide a spatial baseline, representing the surrounding LSTA gradients at the same time as each CI event. No temporal baseline from timesteps without CI was used, as the aim was to assess

https://doi.org/10.5194/egusphere-2026-6670
Preprint. Discussion started: 4 November 2026
© Author(s) 2026. CC BY 4.0 License.

whether the CI location exhibited an anomalous gradient relative to its surroundings. The observed mean initiation gradient was considered significant when it fell outside the central 95% confidence interval of the bootstrap distribution.

4.4 Low-level jets

Next, we classified CI events based on the daily occurrence of low-level jets (LLJs) identified by Jones et al. (2023) over South America during November–March over the period 2001-2020, the austral summer, when convective activity and moisture transport are most frequent over the study region. To assess the influence of LLJs on each CI event, LLJ occurrences were examined within a three-day window encompassing the day before, the day of, and the day after the event. This time window was selected to account for the potential preconditioning effects of LLJs on the convective environment, as these circulations can modulate low-level moisture transport, convergence, and thermodynamic conditions over periods longer than the instantaneous time of CI occurrence (Marengo et al., 2002). The day after the CI event was not considered as a preconditioning period, but was included to provide a symmetric three-day window around each event and to characterize LLJ occurrence immediately before, during, and after CI (see Supplementary Fig. S3). This also provides a consistent three-day period for comparing LLJ occurrence across events, while the potential preconditioning effect is attributed only to LLJs occurring before CI.

We defined geographical regions A (∼5°N–2°S) and B (∼2°S–5°S) as extensions of the LLJ-influenced areas over the eastern flank of the Andes and the Amazon Basin (see Fig. 1a). The Northern LLJ was considered to extend into either region A or region B, but not both simultaneously. In contrast, the Andes LLJ was considered to extend into both regions, whereas the Central LLJ was considered to extend only into region B. Based on these criteria, CI events were classified into four categories: Northern LLJ, Andes LLJ, Central LLJ (see Supplementary Fig. S1 and the study region description), and no Jet. Finally, we quantified the fraction of CI events associated with LLJs and classified them according to wind direction.

4.5 Analyzing rainfall characteristics

Half-hourly, high-quality microwave-only rainfall rate estimates at approximately 10-km spatial resolution from the IMERG final run version 07 dataset (Huffman et al., 2019) were used to analyze the 18-h rainfall evolution following CI events. The 18-h analysis window was selected to encompass the early evolution and organization stages of convective systems following CI events, as convection over the Tropical Andes can persist and evolve over several hours after initiation, including transitions from localized convection to more organized precipitation systems (Chavez and Takahashi, 2017; Poveda et al., 2005). Prior to analyzing rainfall characteristics and spatial patterns, a 100-km radius surrounding each CI event was selected (Fig. 4a). The analysis was then stratified according to wind direction and the presence of LLJs during November- March over the period 2001-2020 (Fig. 7a). This dataset was also used to investigate rainfall properties at the grid-cell level, including: (i) total precipitation, (ii) the timing of peak precipitation, and (iii) the contribution of precipitation occurring at the peak hour to the total accumulated precipitation (Figs. 7b, 8a, and 8b, respectively). Finally, the relationship between total precipitation and the timing of peak precipitation following CI (Fig. 9).

https://doi.org/10.5194/egusphere-2026-6670
Preprint. Discussion started: 4 November 2026
© Author(s) 2026. CC BY 4.0 License.

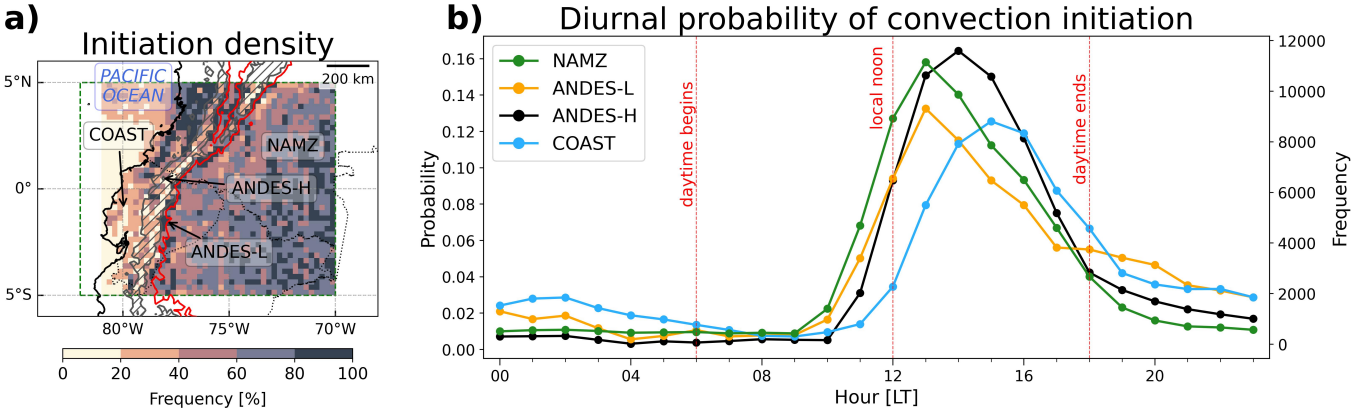


Figure 3. (a) Frequency [%] of detected CI events resampled to a 0.25° x 0.25° grid. (b) Diurnal probability distribution of tracked CI events by four eco-regions (NAMZ, ANDES-H, ANDES-L, and COAST); the red dashed lines from left to right show the start time and the daytime of CI events considered for MODIS LSTAs analysis, local noon.

5 Results

5.1 Tracked convective initiation events

Applying the CI tracking criteria (Section 4.1) across the domain for the period 2001-2020 we identified 111,239 CI events, with 74% occurring in NAMZ, 14.1% in COAST, 8.3% in ANDES-L, and 3.6% in ANDES-H. Fig. 3a presents the spatial distribution of CI frequency, aggregated onto a 0.25° X 0.25° grid, highlighting a maximum over the NAMZ. The diurnal cycle (Fig. 3b) reveals that convection mostly initiates during the early to late afternoon, between noon and 6 pm. The frequency peaks earliest in NAMZ and ANDES-L (1 pm), followed by ANDES-H (2 pm) and COAST (3 pm). After 7 pm, the normalized probability of CI drops below 0.08 and remains low until noon the next day.

CI event durations show differences among eco-regions (Supplementary Table 1), with NAMZ and ANDES-H exhibiting shorter durations, with a median duration of 1 h, whereas ANDES-L and COAST present longer-lasting events, with median durations of 3 h and 6 h, respectively.

5.2 Local land surface and atmospheric conditions and seasonal distribution of CI events

Before examining the environmental conditions, the CI events identified in the previous section (Section 5.1) were further filtered using a $\geq 95\%$ confidence criterion to ensure reliable, cloud-free LST estimates. This resulted in 1906 CI events across the three eco-regions (NAMZ, ANDES-L, and ANDES-H) and all wind directions. Of these, 1371 events (71.9%) were associated with northwesterly (10.2%), northerly (16.8%), northeasterly (27.1%), or easterly (18.6%) flow (Fig. 5a). These 1371 events were subsequently used as the final sample for all analyses presented below. This dominance is also evident in the spatial distribution of events shown in Fig. 5b. Given their substantial contribution, the subsequent analysis focuses exclusively

https://doi.org/10.5194/egusphere-2026-6670
Preprint. Discussion started: 4 November 2026
© Author(s) 2026. CC BY 4.0 License.

on these four wind-direction categories. A bimodal seasonal distribution of CI (Fig. 5c) is evident across all wind directions, with peak frequencies occurring during January–April and September–December. This enhanced CI activity during the two seasonal maxima is consistent with the migration of the ITCZ, which creates conditions favorable for increased atmospheric instability and moisture availability. Additionally, background wind speed exhibits limited variability across wind-direction categories and eco-regions, with a median of 1.2 m s^{-1} across all CI cases (Supplementary Fig. S5).

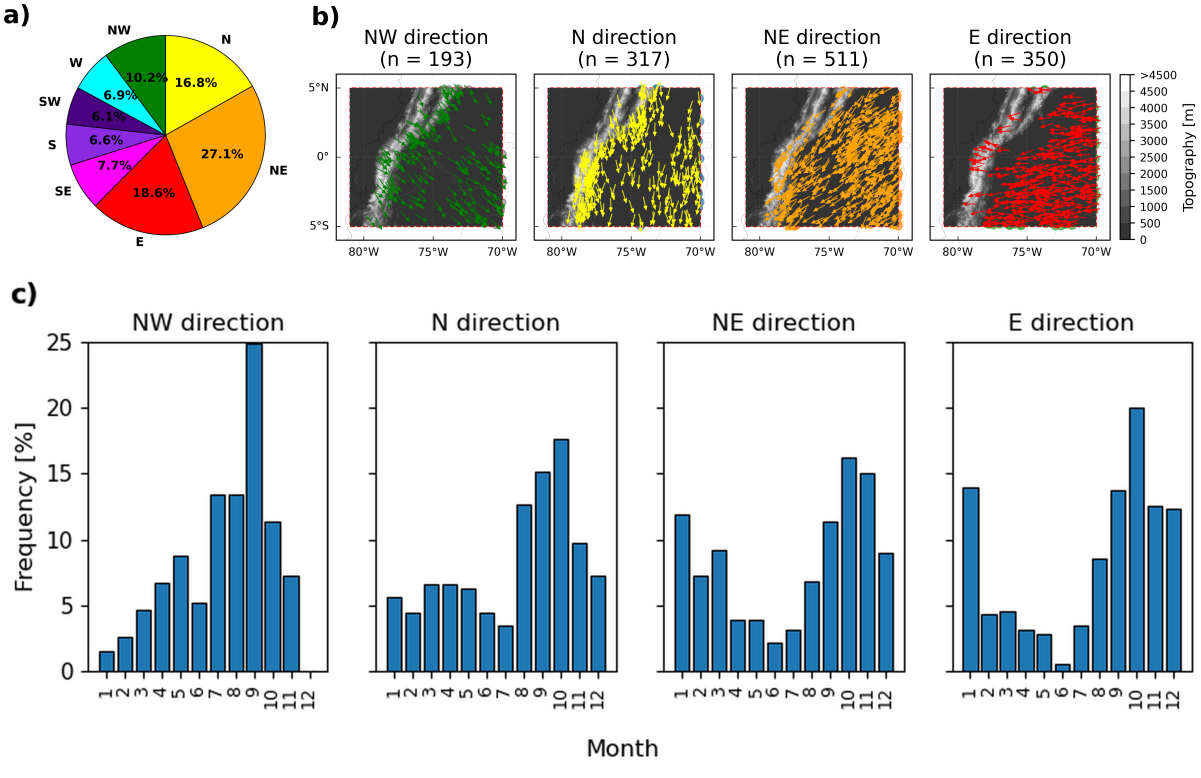


Figure 4. (a) Percentage of CI events, categorized by wind direction. (b) CI cases are categorized by average wind direction in the 2-h before the detected CI time. (c) Seasonal distribution of CI cases, categorized by wind direction, in the 2-h before the detected CI time.

https://doi.org/10.5194/egusphere-2026-6670
Preprint. Discussion started: 4 November 2026
© Author(s) 2026. CC BY 4.0 License.

5.2.1 Topography

Fig. 5a presents elevation cross-sections for 1371 CI events across eco-regions and wind directions, illustrating the potential role of orographic forcing in modulating convection initiation. Over NAMZ, the weak topography gradient suggests negligible orographic control, more visible for NE and E directions, while for NW and N directions the convection initiation region coincides with a transition from higher upwind terrain to lower elevations.

Conversely, in ANDES-L CI occurs at a median elevation of ~ 1.2 km and exhibits two distinct patterns depending on the wind direction. For NW and N events, CI develops along the downslope, suggesting that orographic forcing is not the dominant triggering mechanism. In contrast, NE events are associated with moderate terrain gradients along the slope, indicating a more distributed triggering of convection during upslope ascent. No CI events were identified for E winds in ANDES-L. Easterly flow originating from the Amazonian lowlands approaches the eastern Andean slopes of ANDES-L (1000–2000 m asl) nearly perpendicular to the mountain barrier. Given the steep and complex topography, this cross-barrier flow may be strongly modified and redistributed as it encounters the Andes, with part of the flow potentially being redirected toward higher elevations and ANDES-H, while another fraction may preferentially remain within NAMZ. Such flow redistribution would limit the accumulation and convergence of low-level moisture over ANDES-L and reduce the upward motion necessary to initiate deep convection. Consequently, despite the availability of moisture upstream over the Amazonian lowlands, the near-surface flow configuration over ANDES-L may remain unfavorable for daytime convective initiation.

Over ANDES-H, CI tends to occur near the highest elevations (median ~ 2.5 km), just before the terrain begins to descend, except in the N direction, where a plateau extends approximately 50 km downwind of the CI location. It suggests that sustained orographic lifting along the windward slope of the Andes creates favorable conditions for CI by progressively enhancing moisture convergence and atmospheric instability, as indicated by the strong gradients in the NW and E directions. In contrast, the N and NE cases exhibit only moderate gradients across the CI region. These topographic gradients can enhance low-level convergence and mechanically forced ascent, promoting mechanical lifting and favoring CI. The contrast among wind directions suggests that steeper terrain gradients provide a stronger orographic forcing for CI.

In summary, the low-lying NAMZ exhibits negligible orographic influence, as expected. In ANDES-L, however, orographic forcing may contribute to CI under NE upslope flow, whereas in ANDES-H it is strongest under NW and E flow.

5.2.2 EVI

Regarding vegetation effects (Fig. 5b), represented by the Enhanced vegetation index (EVI) anomalies, no systematic modulation of CI occurrence by wind direction is evident. However, positive EVI anomalies are observed, indicating greener-than-average conditions relative to the corresponding monthly values for each eco-region. This greening signal may primarily reflect enhanced CI activity and associated rainfall. Anomalies are larger in ANDES-H, followed by ANDES-L, and last NAMZ. The anomalies are positively larger simply reflect greater vegetation heterogeneity at higher elevations, reinforcing the observation that vegetation has no distinct influence on CI. Moreover, although instantaneous vegetation cover during CI events is highest over NAMZ, intermediate over ANDES-L, and lowest over ANDES-H (Supplementary Fig. S6), positive EVI anomalies ex-

https://doi.org/10.5194/egusphere-2026-6670
Preprint. Discussion started: 4 November 2026
© Author(s) 2026. CC BY 4.0 License.

hibit an inverse spatial gradient. This apparent contrast arises because, in heterogeneous and sparsely vegetated regions such as ANDES-H, even a small increase in greenness relative to the low instantaneous vegetation cover during CI events can result in a large percentage anomaly. In contrast, over densely vegetated regions such as NAMZ, a comparable increase in greenness corresponds to a much smaller relative change. Thus, the larger positive anomalies observed over ANDES-H primarily reflect the low instantaneous vegetation cover rather than a stronger vegetation–convection feedback.

5.2.3 CAPE and CIN

Fig. 5c presents the distribution of $CAPE$ [J Kg^{-1}] for CI events at different regions and wind directions. Although $CAPE$ values remain relatively modest across all observations (median, 800 [J Kg^{-1}]), observed differences are primarily among regions, whereas differences between directions appear to be minimal. Higher $CAPE$ values are consistently associated with air masses originating over NAMZ, indicating a clear upstream thermodynamic influence on the pre-convective environment and following buoyancy. This signal is weaker over ANDES-L and ANDES-H, where $CAPE$ values are lower and less variable across wind directions, suggesting a comparatively larger role of local topographic forcing. In contrast, CIN exhibits limited variability across wind-direction categories, with a median of 110 [J kg^{-1}] across all cases (Supplementary Fig. S7).

These differences have important implications for convective development. Environments characterized by higher $CAPE$ generally favor more vigorous CI, stronger updrafts, and greater precipitation intensity, potentially supporting longer-lived convective systems that can propagate farther from their initiation regions. Conversely, convection developing under lower-$CAPE$ conditions over ANDES-L and ANDES-H is likely to be more strongly controlled by terrain-induced lifting, resulting in storms of more moderate intensity that remain relatively localized despite frequent triggering. These findings suggest that moisture-rich NAMZ inflow primarily modulates storm intensity and organization, whereas Andean pathways exert a stronger influence on the location and timing of CI.

5.3 Mean surface temperature and moisture anomalies

Having characterized the 111,239 CI events (Section 4.1), we next examined antecedent land surface conditions using MODIS LST observations. Of these, 1,371 occurred within the time window used for the LSTA analysis (Section 4.3); this subset was further filtered to retain valid morning retrievals with a confidence level of at least 95% and sufficient valid-pixel coverage across the analysis transect. Ultimately, 1,371 of these high-quality events were selected by categorizing according to wind direction (Section 4.2) (Fig. 6a) to compute composite mean, primarily concentrated in the NAMZ, ANDES-L, and ANDES-H eco-regions. Composites are computed across the entire region to avoid statistical noise and artifacts caused by small sample sizes within individual eco-regions. The composite analysis of LSTAs patterns (Fig. 6b) reveals that CI tends to occur near the downwind edge of the warmest anomaly co-located with the initiation region, with relatively cooler conditions downwind. Surface thermal patterns, represented by LSTAs, directly reflect antecedent soil moisture deficits that drive local sensible heat gradients. A one-dimensional cross-section along the downwind direction through the CI location (Fig. 6c) indicates that the strongest LSTAs gradient is centered near the initiation point and extends downstream. The mean gradient across 1,371 events is -0.726 K (100 km)$^{-1}$, statistically significant at the 99% confidence level. This structured thermal transition indicates that

https://doi.org/10.5194/egusphere-2026-6670
Preprint. Discussion started: 4 November 2026
© Author(s) 2026. CC BY 4.0 License.

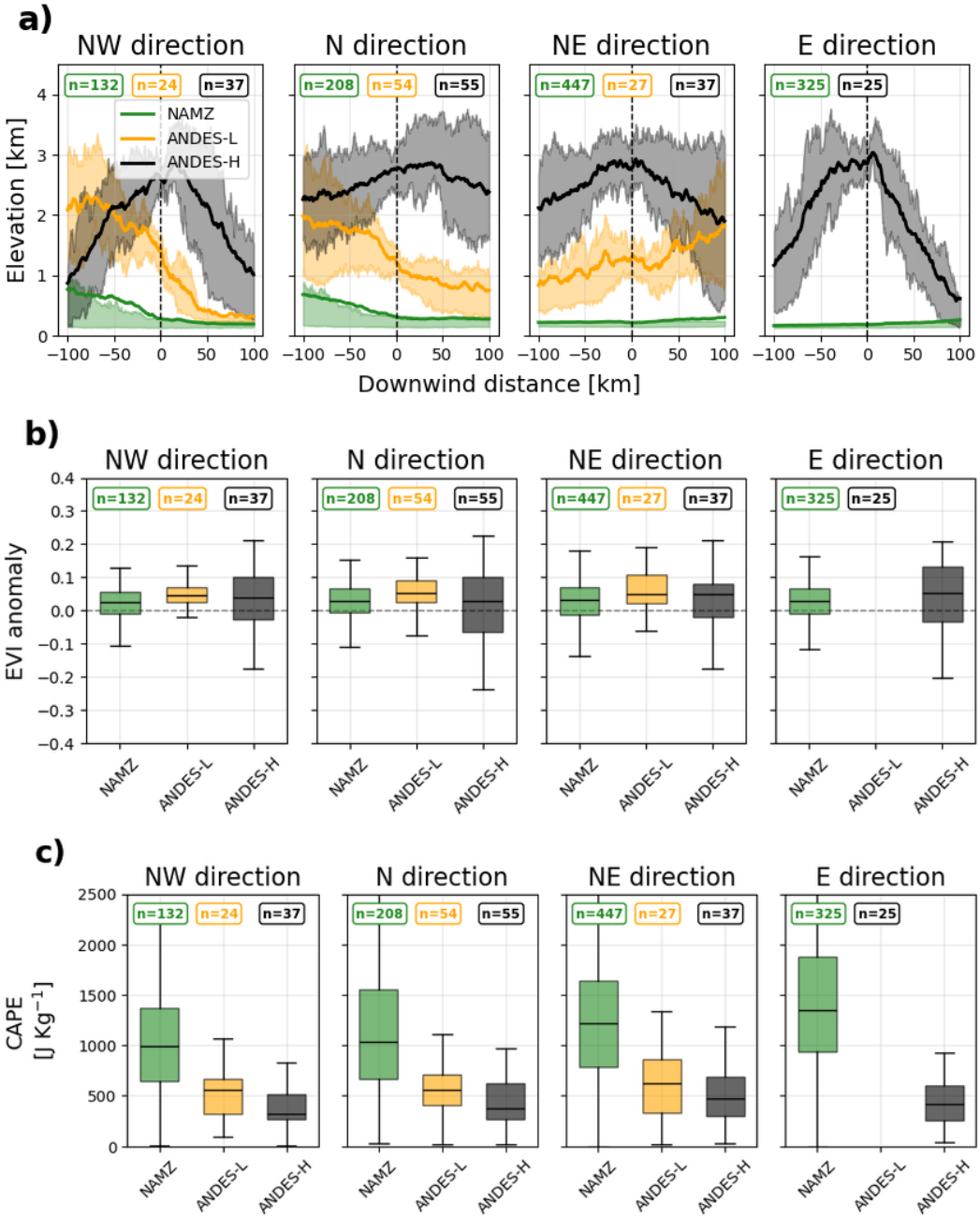


Figure 5. (a) Downwind cross-section of elevation for CI cases by eco-regions, categorized by wind direction during the 2-h before the detected CI time. Shaded areas represent the 25^{th} and 75^{th} percentiles. (b) Boxplots of EVI anomalies for the three eco-regions considering wind direction. (c) Boxplots of convective available potential energy ($CAPE$,[J Kg^{-1}]) for the three eco-regions considering wind direction.

https://doi.org/10.5194/egusphere-2026-6670
Preprint. Discussion started: 4 November 2026
© Author(s) 2026. CC BY 4.0 License.

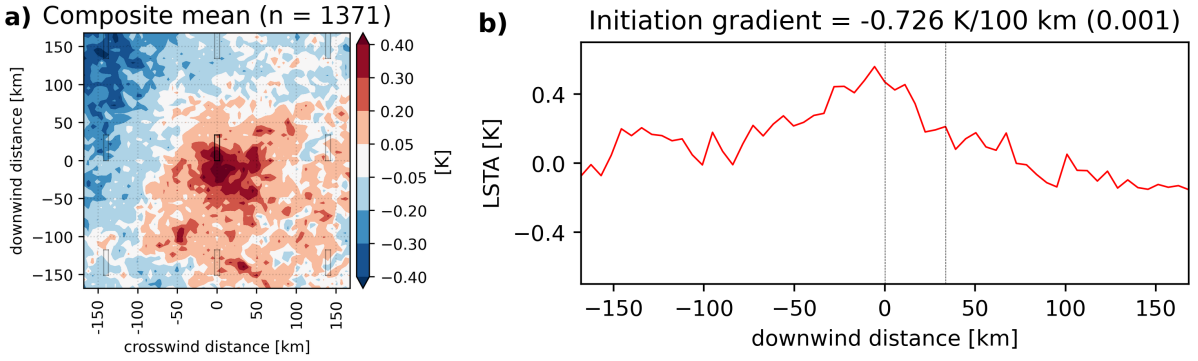


Figure 6. (a) Composite mean land surface temperature anomalies (LSTAs; K) underlying CI cases, where the LSTAs transects for each case were first aligned in the direction of the low-level (10 m) average wind in the 2 h before the detected CI time. The center (0, 0) denotes the initiation location for each case. The black rectangle (10 km x 30 km) at the center is used to calculate the downwind LSTA gradient at the initiation point. Gray rectangles were similarly used to calculate the downwind gradients over non-initiation locations for significance testing. (b) Downwind cross section of mean LSTA for all CI cases (thick red curve). Dashed lines indicate the extent of the box used to calculate the initiation gradient. Note that in (c), the initiation gradient is reported, and the corresponding p-value indicates statistical significance.

convective storms preferentially trigger along the sharp boundary between contrasting surface conditions, where localized gradients enhance low-level convergence and focus the initiation of events.

5.4 Relationship between low-level jets (LLJs) and total precipitation

Building upon the local and regional mechanisms established in the previous sections, the analysis now transitions to examining how continental scale LLJ events modulate the temporal and spatial distribution of CI events across the study area. We evaluate how LLJ-driven moisture transport and dynamics interact with local-scale thermal gradients to govern storm development by analyzing the occurrence of these processes during November–March over the period 2001–2020. The distribution of CI events by LLJ type and wind direction, based on 573 of the 1,371 events analyzed in the previous sections, is presented in Fig. 7a. These 573 events are considered representative of the synoptic-scale environments and their role in modulating convection initiation. Overall, considering northwesterly, northern, northeastern, and easterly wind directions, CI occurrence is partitioned among the Northern LLJ (9.25%), Andes LLJ (25.75%), Central LLJ (37.75%), and no-jet conditions (27.25%). Indicating that 72.75% of identified CI occurs in the presence of LLJs during November-March. The Andes and Central low-level jets exhibit higher frequencies and favorable conditions for moisture transport and CI, particularly during northeasterly (35%) and northerly (46%) flow regimes, respectively. These preferred configurations align closely with the broader directional modulation of convective initiation across the region (NW: 10.2%, N: 16.8%, NE: 27.1%, and E: 18.6%; see Fig. 4a), indicating that the dominant wind sectors driving overall storm frequency are precisely those most effectively coupled with low-level jet transport.

https://doi.org/10.5194/egusphere-2026-6670
Preprint. Discussion started: 4 November 2026
© Author(s) 2026. CC BY 4.0 License.

Fig. 7b shows the total accumulated precipitation within 18–h following CI events, categorized by wind direction and LLJ occurrence, and computed over 100 km radius surrounding the CI locations identified in Fig. 7a. Higher cumulative precipitation values are associated with northern, northeastern, and easterly flow regimes interacting with the Andes and Central LLJs. For instance, total precipitation from N, NE, and E events reaches 356.7 mm under the Andes LLJ and 549.6 mm under the Central LLJ, together accounting for 906.3 mm. In contrast, total precipitation under the Northern LLJ and no-jet conditions is substantially lower, at 91.3 and 248.4 mm, respectively, together accounting for 339.7 mm. Overall, this indicates that convective initiation associated with the Andes and Central LLJs—particularly under northerly, northeasterly, and easterly flow—produces approximately a $\sim$ 3-fold increase in total precipitation compared to Northern LLJ and no-jet conditions. Although no-jet conditions generally yield lower totals overall, they contribute a notable 121.5 mm specifically under northern flow regimes within the Amazon basin, highlighting a localized anomaly driven by terrain convergence and regional moisture recycling independent of large-scale low-level jet forcing.

https://doi.org/10.5194/egusphere-2026-6670
Preprint. Discussion started: 4 November 2026
© Author(s) 2026. CC BY 4.0 License.

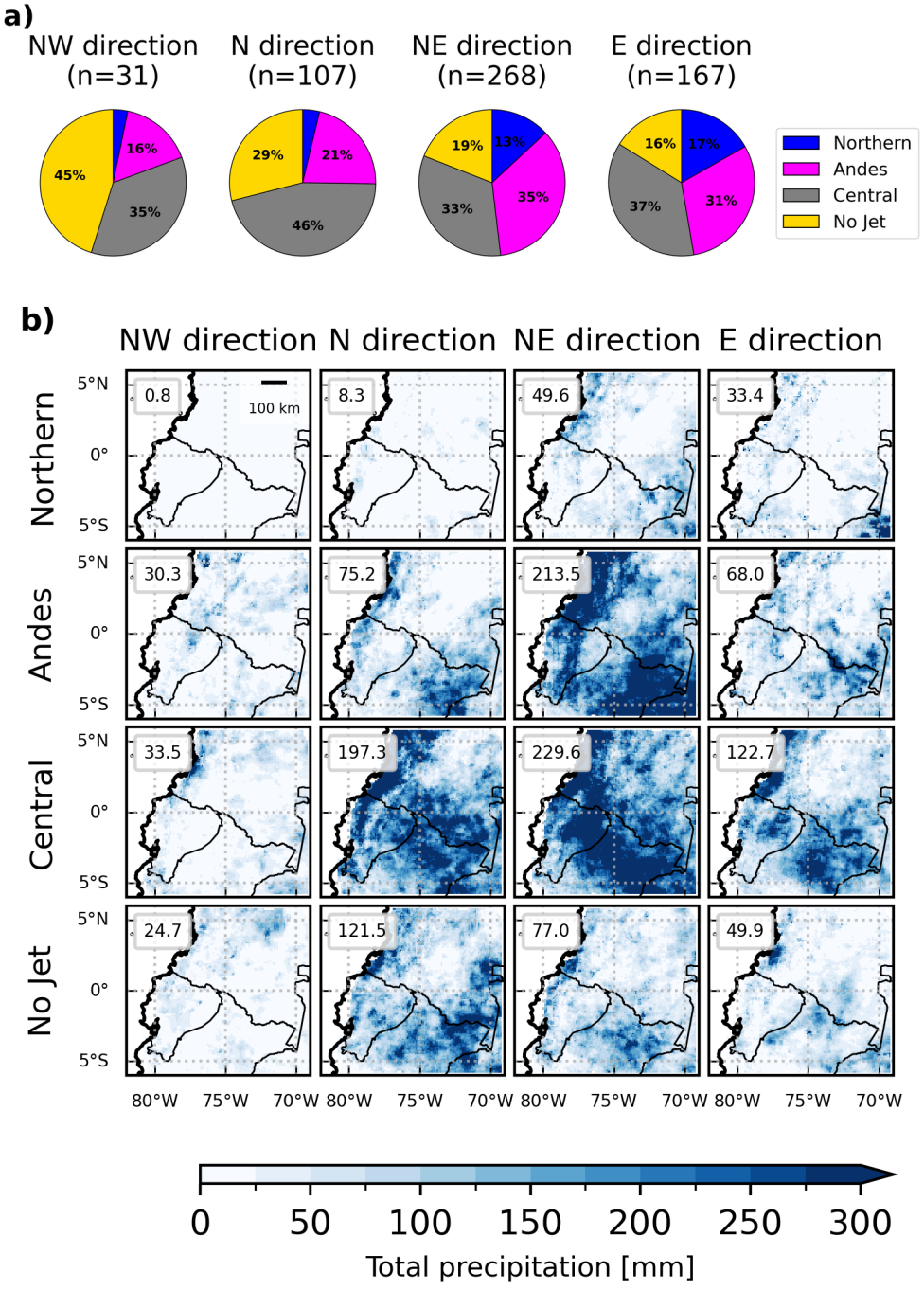


Figure 7. (a) Percentage of CI events associated with LLJs, categorized by wind direction across the NAMZ, ANDES-L, and ANDES-H eco-regions, based on 573 events recorded during November–March 2001–2020. (b) Accumulated precipitation [mm] following 18-hour CI events, LLJs by row and wind direction by column. The spatial average of total precipitation for each panel is indicated.

https://doi.org/10.5194/egusphere-2026-6670
Preprint. Discussion started: 4 November 2026
© Author(s) 2026. CC BY 4.0 License.

5.5 Precipitation properties

Examining the precipitation peak time after CI provides essential insight into the complete convective lifecycle, tracking the transition from initial lower-tropospheric lifting and storm development to mature, precipitating systems. As depicted in Fig. 8a, the precipitation peak occurs on average approximately 4–6 hours after CI across all cases, a lag that clarifies the propagation speed and organization time scales of convective systems in the region and connects surface-forced triggers directly to the delayed maximum of heavy rainfall accumulation. The timing of peak precipitation exhibits strong spatial heterogeneity across the study region and varies substantially with both the propagation direction LLJs regimes. Spatially, Northern LLJ events show the earliest precipitation peaks, particularly over the northern domain (∼2°S–5°N, 74–70°W), whereas Andes LLJ, Central LLJ, and No Jet conditions are characterized by longer delays, especially over the Andean foothills (∼5°S–2°N, 79–75°W) and the central Amazon basin (∼4°S–2°N, 76–72°W). This pattern suggests that both the LLJ regime and convective-system organization exert a strong control on the temporal evolution of precipitation after CI.

Fig. 8b shows the fraction of total accumulated precipitation [%] occurring within the 3-hour period surrounding the precipitation maximum, including the hour preceding and the hour following the peak. For all cases, the peak accounts for 53.1% of the total precipitation. However, this contribution decreases to 42% under northerly, northeasterly, and easterly flow regimes associated with the Andean and Central LLJs, meaning that the remaining 58% of precipitation occurs outside the 3-hour peak window. This relatively balanced partition indicates that both the precipitation maximum and its broader temporal evolution contribute substantially to the total rainfall. Thus, while the peak provides a useful measure of precipitation intensity, considering the precipitation evolution throughout the event is important for capturing its overall rainfall contribution.

Furthermore, we analyze the timing of peak precipitation following CI as a function of total precipitation. We then assess the contribution of peak precipitation accumulated over 3-hour periods to total precipitation across different total precipitation classes, wind directions, and eco-regions, as well as within geographical areas influenced by the Andes and Central LLJs (Fig. 9). Particular attention is given to the Andes and Central LLJs and to northerly (N), northeasterly (NE), and easterly (E) wind directions, which are associated with the highest total precipitation, as shown in Fig. 7b. The inclusion of these two geographical domains is motivated by the influence of the two primary low-level jet (LLJ) systems in South America—the Andes LLJ and the Central LLJ (see Fig. 1a and Supplementary Fig. S1). Their respective areas of influence are based on the spatial characterization of South American LLJs presented by Jones et al. (2023), providing a physically based framework for assessing their potential role in modulating precipitation characteristics. Fig. 9 illustrates differences in precipitation magnitude and peak timing associated with eco-region, wind direction, and LLJ influence. Under the Andes LLJ, the results suggest that higher total precipitation tends to be associated with later peak timing in both geographical areas, with peaks occurring 6–10 h after CI. In Region A, NE winds drive maximum total precipitation, peaking late (8 h post-CI) over ANDES-H (301 mm) and ANDES-L (243 mm), while N and E winds yield lower totals (<150 mm) with earlier peaks (3–7 h). Region B displays an inverse spatial gradient, where NE winds concentrate peak precipitation over NAMZ (280 mm at 8 h post-CI) and ANDES-L (197 mm at 10 h), whereas N and E winds produce under 105 mm and exhibit the earliest peaks overall (3–7 h post-CI).

https://doi.org/10.5194/egusphere-2026-6670
Preprint. Discussion started: 4 November 2026
© Author(s) 2026. CC BY 4.0 License.

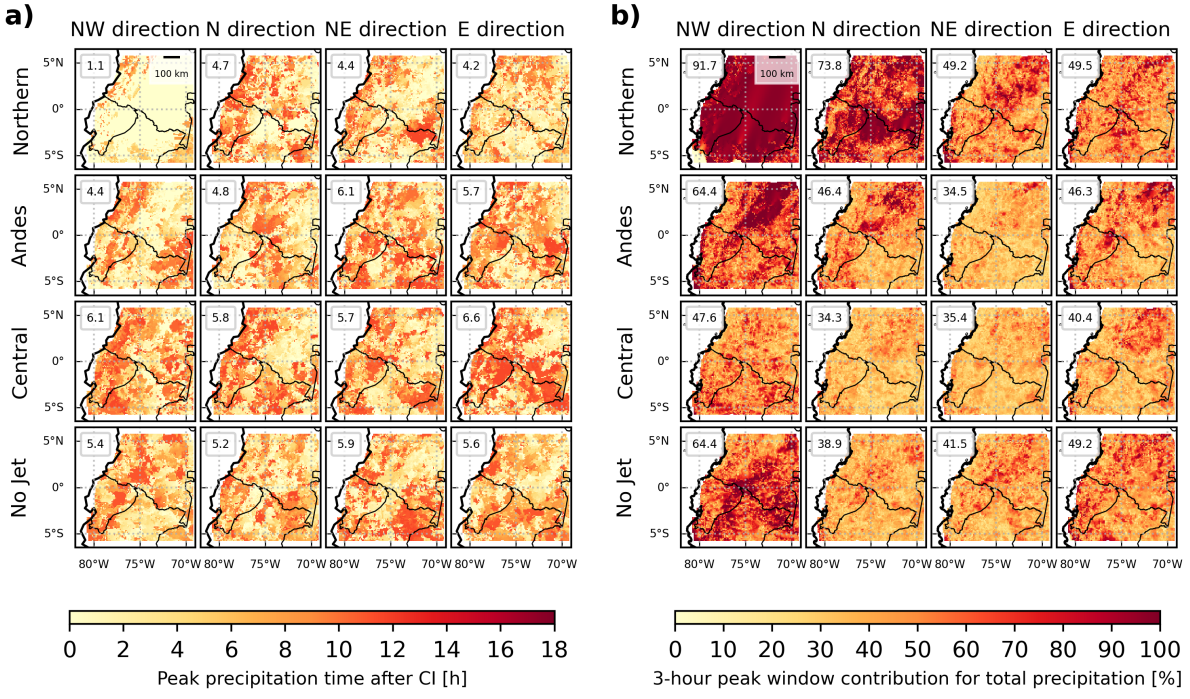


Figure 8. (a) Precipitation peak time [hour] after CI following 18-hour CI events. (b) Contribution of 3-h peak precipitation to total precipitation [%] during the 18-hour after CI. LLJs by row and wind direction by column. The spatial average of the time (hour) and percentage [%] for each panel is indicated.

Across both A and B regions, events with higher total precipitation frequently coincide with moderate 3-h peak contributions (20–40%, represented by medium arrows).

Under the Central LLJ, total precipitation and peak timing display a more decoupled relationship. In Region A, high totals under N and NE winds (178–255 mm) correspond to peak timing clustered between 5 and 9 h post-CI, with ANDES-H exhibiting a late peak (8.5 h) despite a moderate 20–40% peak contribution. In Region B, N and NE winds again shift maximum precipitation toward the lowlands (231 mm over NAMZ), but peak times remain largely uniform across eco-regions (6.5–7.5 h post-CI).

https://doi.org/10.5194/egusphere-2026-6670
Preprint. Discussion started: 4 November 2026
© Author(s) 2026. CC BY 4.0 License.

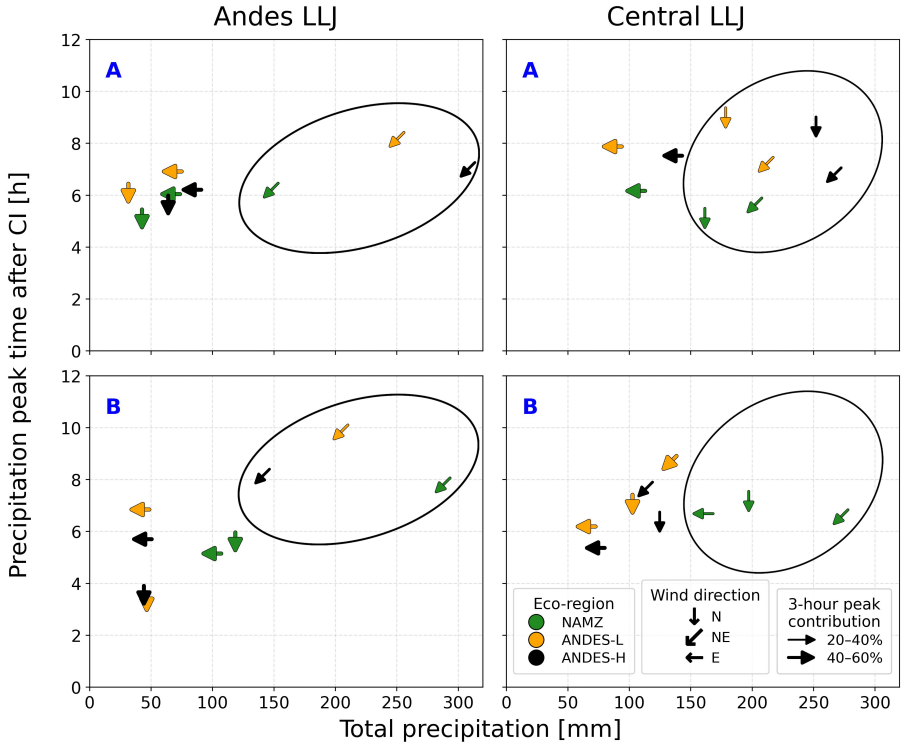


Figure 9. Relationship between total precipitation and the timing of peak precipitation following convective initiation (CI). The ellipses indicate higher rainfall amounts and their corresponding delayed peak times. Rows correspond to the two geographical regions (A and B), while columns correspond to the Andes LLJ and Central LLJ, respectively. Symbols indicate eco-regions (NAMZ, ANDES-L, and ANDES-H), arrow direction denotes the associated wind direction (N, NE, or E), and arrow size represents the contribution of 3-h peak precipitation to total precipitation (20–40% and 40–60%).

https://doi.org/10.5194/egusphere-2026-6670
Preprint. Discussion started: 4 November 2026
© Author(s) 2026. CC BY 4.0 License.

6 Discussion

6.1 What are the conditions associated with CI?

The near-surface circulation associated with CI is predominantly characterized by northwesterly, northerly, northeasterly, and easterly flow regimes, which collectively account for 72.7% or 1371 of all events (1906 events) (Fig. 4). Orographic gradients exert a strong influence on CI occurrence over the ANDES-H and ANDES-L, whereas no discernible orographic control is identified across the NAMZ (Fig. 5a). No strong association was found between CI occurrence and vegetation characteristics (Fig. 5b and Supplementary Fig. S6). This lack of a clear relationship may be attributed to the heterogeneous distribution of land-use and land-cover types across the study region. Although forests are dominant, a substantial proportion of the area is characterized by a combination of woody savanna, grassland, and shrubland, accounting for 13.8% of NAMZ, 9% of ANDES-L, and 26% of ANDES-H (see Supplementary Fig. S8). In terms of thermodynamic instability, as quantified by $CAPE$ and CIN (Fig. 5c and Supplementary Fig. S7, respectively), no clear association with CI occurrence was evident. Across the regions examined, $CAPE$ showed a median value of approximately 800 J kg^{-1} across all wind-direction categories. NAMZ was an exception, exhibiting relatively high $CAPE$ values, reaching approximately 1200 J kg^{-1}. Although these values are relatively low compared with those observed in other mountainous regions, such as the Alps (Feldmann et al., 2025), they represent comparatively high values within the regions examined in this study. This suggests a limited role of these factors in controlling CI variability within the analyzed domain, consistent with previous findings by Campozano et al. (2018). $CAPE$ and CIN may be more relevant in the midlatitudes (Feldmann et al., 2025), whereas tropical convection is more strongly influenced by conditional instability. In particular, the coexistence of a moist boundary layer and a drier layer aloft can generate strong vertical gradients in equivalent potential temperature (θ_e) and moist static energy, potentially playing a key role in CI.

CI events are generally characterized by a positive surface temperature anomaly co-located with the initiation region, followed by relatively cooler conditions downstream (Fig. 6a). Such thermal gradients have been shown to locally enhance vertical wind shear through amplified temperature contrasts that promote convergence in the midlatitudes (Barton et al., 2025). Although wind shear is generally weak in tropical regions, the co-occurrence of strong land surface temperature anomaly (LSTA) gradients and moderate-level flow may enhance local convection-favouring conditions (Taylor et al., 2026). In tropical regions, atmospheric boundaries may further favour CI through the interaction of warm, moist air advected by low-level circulation with relatively colder and drier air downstream of mountainous terrain. The resulting thermodynamic contrast may promote convective instability, further enhancing CI (Houze Jr, 2012; Mapes and Houze Jr, 1993).

A total of 72.75% of CI events occur in conjunction with LLJs, highlighting the substantial contribution of the Central and Andes LLJs to convective development (Fig. 7a). Because LLJs typically transport moisture away from the tropics, moisture convergence is expected near the jet-exit region (Jiménez-Sánchez et al., 2019, 2020). The prevalence of northeasterly (27.1%) and easterly (18.6%) flow therefore suggests an important role for easterly moisture transport and orographic lifting in the observed CI distribution (Fig. 4a).

Despite their potential for enhanced orographic lifting (Fig. 5a), easterly flows are generally associated with drier conditions, potentially explaining the lower precipitation efficiency compared with northerly and northeasterly LLJ regimes (Fig.

https://doi.org/10.5194/egusphere-2026-6670
Preprint. Discussion started: 4 November 2026
© Author(s) 2026. CC BY 4.0 License.

7b). Previous studies have linked easterly flow across the tropical Amazon, particularly Rondônia, to dry-season conditions and enhanced precipitation over the northwestern Amazon (Petersen et al., 2002; Carvalho et al., 2002; Cifelli et al., 2002). These findings suggest that easterly flow can favor CI through orographic lifting while limiting subsequent precipitation development through reduced atmospheric moisture availability compared with moisture-rich LLJ environments (Fig. 7b). The diurnal weakening of LLJs may further reduce moisture export during daytime, increasing local moisture availability for topographic lifting and convective development under conditions of strong CAPE (Fig. 5c).

Notably, the contribution of orography to CI occurrence varies according to the prevailing wind direction and the eco-region of initiation, highlighting distinct interactions between terrain-induced forcing and regional atmospheric circulation patterns, as described below.

1. **Northwesterly direction.** Over the ANDES-H eco-region, CI preferentially occurs near the highest elevations (around 2.5 km), immediately upstream of a pronounced downslope transition associated with a strong orographic gradient. In contrast, orographic effects appear to be negligible over ANDES-L and NAMZ.

2. **Northerly direction.** In the ANDES-H eco-region, CI is associated with a moderate orographic gradient at elevations of approximately 2.5 km, where a plateau extends for nearly 50 km downstream from the initiation location. Orographic influences remain minimal over ANDES-L and NAMZ.

3. **Northeasterly direction.** Moderate topographic gradients are observed over both ANDES-H and ANDES-L, with CI occurring at elevations of approximately 2.5 km and 1.2 km, respectively, whereas the influence of terrain is negligible over NAMZ.

4. **Easterly direction.** Orographic forcing is primarily evident over ANDES-H, where CI is associated with a pronounced terrain gradient, while no significant topographic influence is identified elsewhere.

6.2 What are the characteristics associated with convective precipitation?

CI events associated with the Central and Andes LLJs, under prevailing near-surface northerly, northeasterly, and easterly flow, generate nearly three times more precipitation than events characterized by northwesterly flow or the absence of LLJs (Fig. 7b). Once convection initiates, precipitation reaches its maximum intensity approximately 6-h later and is strongly influenced by low-level wind regimes and the occurrence of LLJs (Fig. 8a). Interestingly, this enhanced precipitation response is characterized by a more persistent and moderate-intensity pattern, consistent with similar findings reported for the southern Ecuadorian Andes by Urdiales-Flores et al. (2025), rather than being concentrated in short-lived, extreme precipitation episodes (Fig. 8b).

Rather than acting independently, orographic forcing and moisture transport interact to shape the spatial distribution of precipitation across the Andes–Amazon transition. Previous modelling studies have shown that regional-scale relief can enhance moisture fluxes toward the Andes, while local topographic features can further channel these flows and modulate the location and intensity of precipitation hotspots (Gutierrez-Villarreal et al., 2025). Further analysis of spatial profiles of equivalent potential temperature (θ_e) and moist static energy could provide additional insight into the thermodynamic conditions gov-

https://doi.org/10.5194/egusphere-2026-6670
Preprint. Discussion started: 4 November 2026
© Author(s) 2026. CC BY 4.0 License.

erning convective development, particularly given their relevance to tropical convection. Our results are consistent with this framework, as the contrasting precipitation regimes across NAMZ, ANDES-L, and ANDES-H vary with the prevailing wind direction and associated LLJ-driven moisture transport. Thus, the regional differences identified here likely reflect the combined effects of terrain-induced lifting and directional moisture transport, rather than the influence of topography alone (Fig. 9). In addition, higher rainfall amounts are observed under northerly flow regimes within the Amazon Basin (Fig. 7a), potentially associated with terrain-induced convergence and regional moisture recycling rather than with large-scale LLJs forcing. Further analysis will investigate whether these events are linked to squall lines, as described by Cohen et al. (1995), by examining the evolution of a subset of cases and comparing them with convective systems previously documented in the Amazon.

6.3 Applications, relevance, limitations and future directions

Our findings have important implications for precipitation modeling, hydrometeorological analysis, and the evaluation of climate models in complex terrain. Incorporating detailed characteristics of severe CI and integrating the observed CI metrics—such as the 3–6-hour peak latency following CI, regional total precipitation thresholds, and dependencies on wind direction—into convection-permitting models could contribute to more realistic representations of precipitation patterns and local topographic controls. In particular, explicitly accounting for topographic structures and the atmospheric mechanisms associated with the Andean–Amazon rainiest zone, as highlighted by Gutierrez-Villarreal et al. (2025), may improve the representation and spatial localization of precipitation hotspots. Similarly, improving the capabilities of flood early warning systems (FEWS) and incorporating the relationships between LLJs regimes and peak precipitation intensity could provide valuable indicators for improving short-term precipitation forecasting, for example, through approaches such as that proposed by Tran et al. (2026). Given the limited observational and process-based studies of CI in this region, the present work provides a valuable baseline for future investigations and contributes to a broader understanding of the mechanisms governing convective development in complex environments. These findings represent an initial step toward characterizing a region that remains relatively unexplored in terms of the mesoscale processes and drivers governing deep convection.

Further advances should address the limitations associated with the quality and uncertainty of satellite-based observations. Although satellite observations and reanalysis datasets covering the period 2001–2020 provide a valuable framework for investigating CI across this data-sparse region, uncertainties in satellite-derived precipitation and convective characteristics may affect the representation of rainfall intensity, spatial distribution, and storm evolution. Nevertheless, established correction procedures were applied and the associated uncertainties were carefully considered, allowing us to identify robust signals in CI processes, their drivers, and associated rainfall characteristics across the region. Future research should investigate how CI and associated precipitation characteristics respond to different land surface and land-cover conditions, particularly across the strong environmental gradients between the Amazon basin and the eastern Andes. Such analyses could provide further insight into the role of land surface heterogeneity and orographic gradients in modulating convective development and precipitation, building on approaches such as those of Gnann et al. (2025).

Precipitation extremes in mountainous regions are expected to respond to climate warming through a combination of thermodynamic and dynamical mechanisms. However, the processes governing convective development and precipitation formation

https://doi.org/10.5194/egusphere-2026-6670
Preprint. Discussion started: 4 November 2026
© Author(s) 2026. CC BY 4.0 License.

in the tropics remain incompletely understood (Gentine et al., 2019; Taylor, 2015), particularly in tropical high-mountain regions, where the interactions among convection, topography, and atmospheric circulation differ substantially from those in midlatitude environments (AlNasser et al., 2026). These interactions can strongly modulate the magnitude, timing, and spatial distribution of precipitation extremes, while changes in large-scale circulation and regional moisture transport may further contribute to heterogeneous responses across complex terrain (Houze Jr, 2004; Pfahl et al., 2017). In this context, the relationships identified in this study between convective initiation, storm evolution, precipitation intensity, and low-level atmospheric circulation provide a useful framework for assessing how these processes may respond to a changing climate. In particular, changes in the frequency, timing, and intensity of CI, together with shifts in moisture transport and low-level jet regimes, could modify the occurrence and characteristics of extreme precipitation events across the Andes–Amazon region. However, the magnitude and even the spatial expression of these changes remain uncertain. Future studies should therefore systematically assess how storm intensity, temporal evolution, and associated moisture transport respond to different warming scenarios. Such analyses would help constrain potential changes in storm trajectories, moisture sources, and transport pathways and, ultimately, reduce uncertainty in projections of extreme precipitation and its future evolution in this climatically and topographically complex region (Nie and Sun, 2022; Claros et al., 2025).

Further research should investigate the environmental differences between CI and non-CI situations and track precipitation from its generation to its eventual location, accounting for storm displacement and the influence of local topography. This would provide a more comprehensive understanding of the links between convective initiation and rainfall distribution. Moreover, the 573 CI events coinciding with LLJs identified during November–March 2001–2020 provide a basis for future analyses using larger event samples to better characterize the spatial patterns and temporal evolution of peak precipitation and assess how LLJs influence rainfall development following CI.

7 Conclusions

This study contributes to the characterization of severe rainfall processes in the Tropical Andes by providing a baseline assessment of convection initiation mechanisms and their subsequent precipitation evolution. Using satellite-based observations and quasi-observed reanalysis datasets, we investigate the atmospheric and surface controls governing convection initiation and identify the main factors influencing precipitation development across the region. Local topography controls the spatial distribution of precipitation intensity by channeling moisture fluxes, while LLJs and wind vectors modulate their magnitude. Our results provide a basis for improving the understanding of rainfall variability and storm development in the Andean region, offering valuable information for the refinement of forecasting approaches and early warning systems. Future research should focus on integrating high-resolution atmospheric observations with advanced satellite-based datasets and dynamical analyses to further investigate the physical mechanisms controlling convection and precipitation, particularly under the influence of a changing climate. These efforts will contribute to a deeper understanding of mountain hydrological cycles and help inform sustainable water resource management strategies across the Andes and other mountainous regions worldwide.

https://doi.org/10.5194/egusphere-2026-6670
Preprint. Discussion started: 4 November 2026
© Author(s) 2026. CC BY 4.0 License.

These results suggest a characteristic timescale of approximately 4–6 hours for convective systems to develop and reach a sufficiently mature stage to produce intense precipitation. Once mature, however, a large fraction of the accumulated precipitation is concentrated within approximately one hour around the precipitation peak. This temporal concentration provides a potentially useful timescale for anticipating the transition from convective development to peak precipitation, with implications for the timing of precipitation nowcasting and the issuance of warnings.

Code availability. Code and data arrays for the main figures are available at https://doi.org/10.5281/zenodo.21838492

Data availability. Unprocessed data are available from the following sources:

- Precipitation: GPM-IMERG (https://doi.org/10.5067/GPM/IMERG/3B-HH/06).
- Brightness temperature: GPM-MERGIR (https://disc.gsfc.nasa.gov/datasets/GPM_MERGIR_1/summary).
- Land water mask: MOD44WV (https://lpdaac.usgs.gov/products/mod44wv006/).
- Land surface temperature (LST): MOD11C (https://lpdaac.usgs.gov/products/mod11c1v061/).
- Land-use and land-cover (LULC): MCD12C1 (https://doi.org/10.5067/MODIS/MCD12C1.006)
- Topography: GMTED2010 (https://www.usgs.gov/coastalchanges-and-impacts/gmted2010).
- Enhanced vegetation index (EVI): MOD13C (https://lpdaac.usgs.gov/products/mod13c2v006/).
- ERA5 pressure levels (https://doi.org/10.24381/cds.bd0915c6).
- ERA5 single levels (https://doi.org/10.24381/cds.adbb2d47).

Author contributions. DUF, FD, DC, and NP designed the study. DUF conducted the analyses, produced the visualisations, and wrote the paper. GM, JC, and LMVC advised DUF during the project. All coauthors revised and edited the paper.

Competing interests. The authors declare no conflicts of interest.

Acknowledgements. Diego Urdiales-Flores was supported by the Swiss Government Excellence Scholarship 2023.0395 as well as the Commission for Research Expertise at the University of Lausanne through the Mobility fellowship-MD-0117 for a 6-month visit at the University of Illinois Urbana–Champaign. Nadav Peleg was supported by the Swiss National Science Foundation (SNSF), Grant 194649 (”Rainfall and floods in future cities”).

https://doi.org/10.5194/egusphere-2026-6670
Preprint. Discussion started: 4 November 2026
© Author(s) 2026. CC BY 4.0 License.

References

AlNasser, F., Gianotti, D., and Entekhabi, D.: Soil moisture impact on convective initiation, Water Resources Research, 62, e2025WR042 329, https://doi.org/10.1029/2025WR042329, 2026.

Barton, E., Taylor, C., Klein, C., Harris, P., and Meng, X.: Observed soil moisture impact on strong convection over mountainous Tibetan Plateau, Journal of Hydrometeorology, 22, 561–572, https://doi.org/10.1175/JHM-D-20-0129.1, 2021.

Barton, E. J., Klein, C., Taylor, C. M., Marsham, J., Parker, D. J., Maybee, B., Feng, Z., and Leung, L. R.: Soil moisture gradients strengthen mesoscale convective systems by increasing wind shear, Nature Geoscience, 18, 330–336, https://doi.org/10.1038/s41561-025-01666-8, 2025.

Bedoya-Soto, J. and Poveda, G.: Moisture recycling in the Colombian Andes, Water Resources Research, 60, e2022WR033 601, https://doi.org/10.1029/2022WR033601, 2024.

Bendix, J.: Precipitation dynamics in Ecuador and northern Peru during the 1991/92 El Niño: a remote sensing perspective, International Journal of Remote Sensing, 21, 533–548, https://doi.org/10.1080/014311600210731, 2000.

Bendix, J., Rollenbeck, R., Göttlicher, D., and Cermak, J.: Cloud occurrence and cloud properties in Ecuador, Climate Research, 30, 133–147, https://doi.org/10.3354/cr030133, 2006.

Bendix, J., Trachte, K., Cermak, J., Rollenbeck, R., and Nauß, T.: Formation of convective clouds at the foothills of the tropical eastern Andes (South Ecuador), Journal of Applied Meteorology and Climatology, 48, 1682–1695, https://doi.org/10.1175/2009JAMC2078.1, 2009.

Bennett, L. J., Browning, K. A., Blyth, A. M., Parker, D. J., and Clark, P. A.: A review of the initiation of precipitating convection in the United Kingdom, Quarterly Journal of the Royal Meteorological Society: A journal of the atmospheric sciences, applied meteorology and physical oceanography, 132, 1001–1020, https://doi.org/10.1029/2024JD042108, 2006.

Benoit, L., Koch, E., Peleg, N., and Mariethoz, G.: Precipitation-elevation relationship: Non-linearity and space–time variability prevail in the Swiss Alps, Journal of Hydrology X, 25, 100 186, https://doi.org/10.1016/j.hydroa.2024.100186, 2024.

Bieliński, T.: A parallax shift effect correction based on cloud height for geostationary satellites and radar observations, Remote Sensing, 12, 365, https://doi.org/10.3390/rs12030365, 2020.

Campozano, L., Trachte, K., Célleri, R., Samaniego, E., Bendix, J., Albuja, C., and Mejia, J. F.: Climatology and teleconnections of mesoscale convective systems in an Andean basin in southern Ecuador: The case of the Paute basin, Advances in Meteorology, 2018, 4259 191, https://doi.org/10.1155/2018/4259191, 2018.

Carroll, M., DiMiceli, C., Wooten, M., Hubbard, A., Sohlberg, R., and Townshend, J.: MODIS/Terra Land Water Mask Derived from MODIS and SRTM L3 Global 250 m SIN Grid V006, https://catalog.data.gov/dataset/modis-terra-land-water-mask-derived-from-modis-and-srtm-l3-global-250m-sin-grid-v006, data set, accessed 27 July 2026, 2017.

Carvalho, L. M., Jones, C., and Silva Dias, M. A.: Intraseasonal large-scale circulations and mesoscale convective activity in tropical South America during the TRMM-LBA campaign, Journal of Geophysical Research: Atmospheres, 107, LBA–9, https://doi.org/10.1029/2001JD000745, 2002.

Célleri, R., Willems, P., Buytaert, W., and Feyen, J.: Space–time rainfall variability in the Paute basin, Ecuadorian Andes, Hydrological Processes: An International Journal, 21, 3316–3327, https://doi.org/10.1002/hyp.6575, 2007.

Chavez, S. P. and Takahashi, K.: Orographic rainfall hot spots in the Andes-Amazon transition according to the TRMM precipitation radar and in situ data, Journal of Geophysical Research: Atmospheres, 122, 5870–5882, https://doi.org/10.1002/2016JD026282, 2017.

https://doi.org/10.5194/egusphere-2026-6670
Preprint. Discussion started: 4 November 2026
© Author(s) 2026. CC BY 4.0 License.

Chen, J., Dai, A., Zhang, Y., and Rasmussen, K. L.: Changes in convective available potential energy and convective inhibition under global warming, Journal of Climate, 33, 2025–2050, https://doi.org/10.1175/JCLI-D-19-0461.1, 2020.

Chug, D., Dominguez, F., Taylor, C. M., Klein, C., and Nesbitt, S. W.: Dry-to-wet soil gradients enhance convection and rainfall over subtropical South America, Journal of Hydrometeorology, 24, 1563–1581, https://doi.org/10.1175/JHM-D-23-0031.1, 2023.

Cifelli, R., Petersen, W. A., Carey, L. D., Rutledge, S. A., and da Silva Dias, M. A.: Radar observations of the kinematic, microphysical, and precipitation characteristics of two MCSs in TRMM LBA, Journal of Geophysical Research: Atmospheres, 107, LBA–44, https://doi.org/10.1029/2000JD000264, 2002.

Claros, E., Dominguez, F., and Liu, C.: Moisture sources of precipitation using convection-permitting simulations: A study over South America, Geophysical Research Letters, 52, e2025GL118 806, https://doi.org/10.1029/2025GL118806, 2025.

Cohen, J. C., Silva Dias, M. A., and Nobre, C. A.: Environmental conditions associated with Amazonian squall lines: A case study, Monthly weather review, 123, 3163–3174, https://scispace.com/pdf/environmental-conditions-associated-with-amazonian-squall-mldufhff5m.pdf, 1995.

Didan, K.: MOD13C2 MODIS/Terra Vegetation Indices Monthly L3 Global 0.05Deg CMG V006, https://doi.org/10.5067/MODIS/MOD13C2.006, data set, accessed 27 July 2026, 2015.

Dominguez, F., Rasmussen, R., Liu, C., Ikeda, K., Prein, A., Varble, A., Arias, P. A., Bacmeister, J., Bettolli, M. L., Callaghan, P., et al.: Advancing South American Water and Climate Science through Multidecadal Convection-Permitting Modeling, Bulletin of the American Meteorological Society, 105, E32–E44, https://doi.org/10.1175/BAMS-D-22-0226.1, 2024.

Espinoza, J. C., Garreaud, R., Poveda, G., Arias, P. A., Molina-Carpio, J., Masiokas, M., Viale, M., and Scaff, L.: Hydroclimate of the Andes part I: main climatic features, Frontiers in Earth Science, 8, 64, https://doi.org/10.3389/feart.2020.00064, 2020.

Fassoni-Andrade, A. C., Fleischmann, A. S., Papa, F., Paiva, R. C. D. d., Wongchuig, S., Melack, J. M., Moreira, A. A., Paris, A., Ruhoff, A., Barbosa, C., et al.: Amazon hydrology from space: scientific advances and future challenges, Reviews of Geophysics, 59, e2020RG000 728, https://doi.org/10.1029/2020RG000728, 2021.

Feldmann, M., Domeisen, D. I., and Martius, O.: A pan-European analysis of large-scale drivers of severe convective outbreaks, Weather and Climate Dynamics, 6, 1089–1106, https://doi.org/10.5194/wcd-6-1089-2025, 2025.

Fernandez-Palomino, C. A., Hattermann, F. F., Krysanova, V., Lobanova, A., Vega-Jácome, F., Lavado, W., Santini, W., Aybar, C., and Bronstert, A.: A novel high-resolution gridded precipitation dataset for Peruvian and Ecuadorian watersheds: Development and hydrological evaluation, Journal of Hydrometeorology, 23, 309–336, https://doi.org/10.1175/JHM-D-20-0285.1, 2022.

Fowler, H. J., Ali, H., Allan, R. P., Ban, N., Barbero, R., Berg, P., Blenkinsop, S., Cabi, N. S., Chan, S., Dale, M., et al.: Towards advancing scientific knowledge of climate change impacts on short-duration rainfall extremes, Philosophical Transactions of the Royal Society A, 379, 20190 542, https://doi.org/10.1098/rsta.2019.0542, 2021.

Gentine, P., Massmann, A., Lintner, B. R., Hamed Alemohammad, S., Fu, R., Green, J. K., Kennedy, D., and Vilà-Guerau de Arellano, J.: Land–atmosphere interactions in the tropics–a review, Hydrology and Earth System Sciences, 23, 4171–4197, https://doi.org/10.5194/hess-23-4171-2019, 2019.

GMTED: Global Multi-resolution Terrain Elevation Data 2010 (GMTED2010), https://www.usgs.gov/coastal-changes-and-impacts/gmted2010, 2010.

Gnann, S., Baldwin, J. W., Cuthbert, M. O., Gleeson, T., Schwanghart, W., and Wagener, T.: The influence of topography on the global terrestrial water cycle, Reviews of Geophysics, 63, e2023RG000 810, https://doi.org/10.1029/2023RG000810, 2025.

GPM-IMERG: GPM-IMERG half-hourly precipitation retrieval, [Dataset], https://gpm.nasa.gov/data/imerg, 2023.

https://doi.org/10.5194/egusphere-2026-6670
Preprint. Discussion started: 4 November 2026
© Author(s) 2026. CC BY 4.0 License.

GPM-MERGIR: GPM-IMERG half-hourly brightness temperature observations, [Dataset], https://disc.gsfc.nasa.gov/datasets/GPM_MERGIR_1/summary, 2023.

Gupta, S., Wang, D., Giangrande, S. E., Biscaro, T. S., and Jensen, M. P.: Lifecycle of updrafts and mass flux in isolated deep convection over the Amazon rainforest: insights from cell tracking, Atmospheric chemistry and physics, 24, 4487–4510, https://doi.org/10.5194/acp-24-4487-2024, 2024.

Gutierrez-Villarreal, R. A., Junquas, C., Espinoza, J.-C., Baby, P., and Armijos, E.: Influence of local topographic structures on the atmospheric mechanisms related to the Andean-Amazon rainiest zone, Atmospheric Research, 320, 108 068, https://doi.org/10.1016/j.atmosres.2025.108068, 2025.

Hersbach, H., Bell, B., Berrisford, P., Hirahara, S., Horányi, A., Muñoz-Sabater, J., Nicolas, J., Peubey, C., Radu, R., Schepers, D., et al.: The ERA5 global reanalysis, Quarterly journal of the royal meteorological society, 146, 1999–2049, https://doi.org/10.1002/qj.3803, 2020.

Houze Jr, R. A.: Mesoscale convective systems, Reviews of Geophysics, 42, https://doi.org/10.1029/2004RG000150, 2004.

Houze Jr, R. A.: Orographic effects on precipitating clouds, Reviews of Geophysics, 50, https://doi.org/10.1029/2011RG000365, 2012.

Huffman, G. J., Stocker, E. F., Bolvin, D. T., Nelkin, E. J., and Tan, J.: GPM IMERG Final Precipitation L3 Half Hourly 0.1 Degree x 0.1 Degree V07, https://doi.org/10.5067/GPM/IMERG/3B-HH/06, accessed 4 April 2026, 2019.

Imfeld, N., Sedlmeier, K., Gubler, S., Correa Marrou, K., Davila, C. P., Huerta, A., Lavado-Casimiro, W., Rohrer, M., Scherrer, S. C., and Schwierz, C.: A combined view on precipitation and temperature climatology and trends in the southern Andes of Peru, International journal of Climatology, 41, 679–698, https://doi.org/10.1002/joc.6645, 2021.

Janowiak, J. E., Kousky, V. E., and Joyce, R. J.: Diurnal cycle of precipitation determined from the CMORPH high spatial and temporal resolution global precipitation analyses, Journal of Geophysical Research: Atmospheres, 110, https://doi.org/10.1029/2005JD006156, 2005.

Jiménez-Sánchez, G., Markowski, P. M., Jewtoukoff, V., Young, G. S., and Stensrud, D. J.: The Orinoco low-level jet: an investigation of its characteristics and evolution using the WRF model, Journal of Geophysical Research: Atmospheres, 124, 10 696–10 711, https://agupubs.onlinelibrary.wiley.com/doi/full/10.1029/2019JD030934, 2019.

Jiménez-Sánchez, G., Markowski, P. M., Young, G. S., and Stensrud, D. J.: The Orinoco low-level jet: An investigation of its mechanisms of formation using the WRF model, Journal of Geophysical Research: Atmospheres, 125, e2020JD032 810, https://agupubs.onlinelibrary.wiley.com/doi/full/10.1029/2020JD032810, 2020.

Jones, C., Mu, Y., Carvalho, L. M., and Ding, Q.: The South America Low-Level Jet: form, variability and large-scale forcings, npj Climate and Atmospheric Science, 6, 175, https://doi.org/10.1038/s41612-023-00501-4, 2023.

Kirshbaum, D. J. and Durran, D. R.: Factors governing cellular convection in orographic precipitation, Journal of the atmospheric Sciences, 61, 682–698, https://doi.org/10.1175/1520-0469(2004)061<0682:FGCCIO>2.0.CO;2, 2004.

Lin, Y.-L.: Dynamics of orographic precipitation, in: McGraw-Hill 2005 Yearbook of Science & Technology, pp. 248–250, McGraw Hill, 2005.

Liu, C., Ikeda, K., Dominguez, F., Prein, A. F., Rasmussen, R. M., Zhang, Z., Xue, L., Neale, R. B., Chun, K. P., He, C., et al.: Multi-decadal convection permitting dynamical downscaling of current and future climates over South America, Climate Dynamics, 64, 435, https://doi.org/10.1007/s00382-026-08376-w, 2026.

Mapes, B. E. and Houze Jr, R. A.: Cloud clusters and superclusters over the oceanic warm pool, Monthly Weather Review, 121, 1398–1416, https://doi.org/10.1175/1520-0493(1993)121<1398:CCASOT>2.0.CO;2, 1993.

https://doi.org/10.5194/egusphere-2026-6670
Preprint. Discussion started: 4 November 2026
© Author(s) 2026. CC BY 4.0 License.

Marengo, J. A., Douglas, M. W., and Silva Dias, P. L.: The South American low-level jet east of the Andes during the 1999 LBA-TRMM and LBA-WET AMC campaign, Journal of Geophysical Research: Atmospheres, 107, LBA–47, https://doi.org/10.1029/2001JD001188, 2002.

MODIS/Terra (MOD11C1): MODIS/Terra Land Surface Temperature/Emissivity Daily L3 Global 0.05Deg CMG V061 (MOD11C1), https://lpdaac.usgs.gov/products/mod11c1v061/, version 6.1, 2021.

MODIS/Terra (MOD13C2): MODIS/Terra Vegetation Indices Monthly L3 Global 0.05Deg CMG V006 (MOD13C2), https://lpdaac.usgs.gov/products/mod13c2v006/, dataset last updated 22 June 2026; catalog last checked 23 June 2026, 2023.

Mu, Y., Jones, C., Carvalho, L. M., Xue, L., Liu, C., and Ding, Q.: Pacific decadal oscillation and ENSO forcings of northerly low-level jets in South America, npj Climate and Atmospheric Science, 7, 297, https://doi.org/10.1038/s41612-024-00852-6, 2024.

Mu, Y., Jones, C., Carvalho, L. M., Kukulies, J., Prein, A. F., Xue, L., and Liu, C.: Impacts of northerly low-level jets on mesoscale convective systems east of the Andes, Journal of Geophysical Research: Atmospheres, 130, e2025JD043 842, https://agupubs.onlinelibrary.wiley.com/doi/10.1029/2025JD043842, 2025.

Nie, Y. and Sun, J.: Moisture sources and transport for extreme precipitation over Henan in July 2021, Geophysical Research Letters, 49, e2021GL097 446, https://doi.org/10.1029/2021GL097446, 2022.

Paccini, L. and Schiro, K. A.: Influence of soil moisture on the development of organized convective systems in South America, Journal of Geophysical Research: Atmospheres, 130, e2024JD042 108, https://doi.org/10.1029/2024JD042108, 2025.

Peleg, N., Koukoula, M., and Marra, F.: A 2° C warming can double the frequency of extreme summer downpours in the Alps, npj Climate and Atmospheric Science, 8, 216, https://doi.org/10.1038/s41612-025-01081-1, 2025.

Pepin, N., Bradley, R. S., Diaz, H. F., Baraer, M., Caceres, E. B., Forsythe, N., Fowler, H., Greenwood, G., Hashmi, M. Z., Liu, X. D., and others: Elevation-dependent warming in mountain regions of the world, Nature Climate Change, 5, 424–430, https://doi.org/https://doi.org/10.1038/nclimate2563, 2015.

Pepin, N., Arnone, E., Gobiet, A., Haslinger, K., Kotlarski, S., Notarnicola, C., Palazzi, E., Seibert, P., Serafin, S., Schöner, W., et al.: Climate changes and their elevational patterns in the mountains of the world, Reviews of Geophysics, 60, e2020RG000 730, https://doi.org/10.1029/2020RG000730, 2022.

Petersen, W. A., Nesbitt, S. W., Blakeslee, R. J., Cifelli, R., Hein, P., and Rutledge, S. A.: TRMM observations of intraseasonal variability in convective regimes over the Amazon, Journal of Climate, 15, 1278–1294, https://doi.org/10.1175/1520-0442(2002)015<1278:TOOIVI>2.0.CO;2, 2002.

Petrova, I. Y., Miralles, D. G., Van Heerwaarden, C. C., and Wouters, H.: Relation between convective rainfall properties and antecedent soil moisture heterogeneity conditions in North Africa, Remote Sensing, 10, 969, https://doi.org/10.3390/rs10060969, 2018.

Pfahl, S., O'Gorman, P. A., and Fischer, E. M.: Understanding the regional pattern of projected future changes in extreme precipitation, Nature Climate Change, 7, 423–427, https://doi.org/10.1038/nclimate3287, 2017.

Pielke, R. A., Pitman, A., Niyogi, D., Mahmood, R., McAlpine, C., Hossain, F., Goldewijk, K. K., Nair, U., Betts, R., Fall, S., et al.: Land use/land cover changes and climate: modeling analysis and observational evidence, Wiley Interdisciplinary Reviews: Climate Change, 2, 828–850, https://doi.org/10.1002/wcc.144, 2011.

Poveda, G., Mesa, O. J., Salazar, L. F., Arias, P. A., Moreno, H. A., Vieira, S. C., Agudelo, P. A., Toro, V. G., and Alvarez, J. F.: The diurnal cycle of precipitation in the tropical Andes of Colombia, Monthly Weather Review, 133, 228–240, https://doi.org/10.1175/MWR-2853.1, 2005.

https://doi.org/10.5194/egusphere-2026-6670
Preprint. Discussion started: 4 November 2026
© Author(s) 2026. CC BY 4.0 License.

Prein, A. F., Mooney, P. A., and Done, J. M.: The multi-scale interactions of atmospheric phenomenon in mean and extreme precipitation, Earth's Future, 11, e2023EF003 534, https://doi.org/10.1029/2023EF003534, 2023.

Rasmussen, K. L. and Houze Jr, R.: Convective initiation near the Andes in subtropical South America, Monthly Weather Review, 144, 2351–2374, https://doi.org/10.1175/MWR-D-15-0058.1, 2016.

Robledo, V., Henao, J. J., Mejía, J. F., Ramírez-Cardona, Á., Hernández, K. S., Gómez-Ríos, S., and Rendón, Á. M.: Climatological tracking and lifecycle characteristics of mesoscale convective systems in northwestern South America, Journal of Geophysical Research: Atmospheres, 129, e2024JD041 159, https://doi.org/10.1029/2024JD041159, 2024.

Rotach, M. W., Serafin, S., Ward, H. C., Arpagaus, M., Colfescu, I., Cuxart, J., De Wekker, S. F., Grubišic, V., Kalthoff, N., Karl, T., et al.: A collaborative effort to better understand, measure, and model atmospheric exchange processes over mountains, Bulletin of the American Meteorological Society, 103, E1282–E1295, https://doi.org/10.1175/BAMS-D-21-0232.1, 2022.

Serafin, S., Rotach, M. W., Arpagaus, M., et al.: Multi-scale Transport and Exchange Processes in the Atmosphere over Mountains: Programme and Experiment, Innsbruck University Press, https://doi.org/10.15203/99106-003-1, 2020.

Staal, A., Tuinenburg, O. A., Bosmans, J. H., Holmgren, M., van Nes, E. H., Scheffer, M., Zemp, D. C., and Dekker, S. C.: Forest-rainfall cascades buffer against drought across the Amazon, Nature Climate Change, 8, 539–543, https://doi.org/10.1038/s41558-018-0177-y, 2018.

Taylor, C. M.: Detecting soil moisture impacts on convective initiation in Europe, Geophysical Research Letters, 42, 4631–4638, https://doi.org/10.1002/2015GL064030, 2015.

Taylor, C. M., de Jeu, R. A., Guichard, F., Harris, P. P., and Dorigo, W. A.: Afternoon rain more likely over drier soils, Nature, 489, 423–426, https://doi.org/10.1038/nature11377, 2012.

Taylor, C. M., Klein, C., Barton, E. J., Hahn, S., and Wagner, W.: Wind shear enhances soil moisture influence on rapid thunderstorm growth, Nature, 651, 116–121, https://doi.org/10.1038/s41586-025-10045-7, 2026.

Thornton, J. M., Palazzi, E., Pepin, N. C., Cristofanelli, P., Essery, R., Kotlarski, S., Giuliani, G., Guigoz, Y., Kulonen, A., Pritchard, D., Li, X., J., H., Fowler, Randin, C. F., Shahgedanova, M., Steinbacher, M., Zebisch, M., Carolina, and Adler: Toward a definition of essential mountain climate variables, One Earth, 4, 805–827, https://doi.org/https://doi.org/10.1016/j.oneear.2021.05.005, 2021.

Tran, V. N., Huan, X., Antar, A. D., Banovic, N., Bednar, J. H., Bergt, S. M., Cheng, C., Dominguez, F., Fatichi, S., Gonzalez, R., et al.: Reimagining how flood warnings can inform decision-making and community actions, Earth's Future, 14, e2026EF008 857, https://doi.org/10.1029/2026EF008857, 2026.

Urdiales, D., Meza, F., Gironás, J., and Gilabert, H.: Improving stochastic modelling of daily rainfall using the ENSO index: Model development and application in Chile, Water, 10, 145, https://doi.org/10.3390/w10020145, 2018.

Urdiales-Flores, D., Célleri, R., Mariéthoz, G., Bendix, J., and Peleg, N.: Heavy rainfall patterns and high streamflow dynamics in the southern Ecuadorian Andes, Journal of Hydrometeorology, 26, 725–739, https://doi.org/10.1175/JHM-D-24-0105.1, 2025.

Urdiales-Flores, D., Koukoula, M., Prein, A. F., Jan De Vries, A., Mariéthoz, G., Bendix, J., Dominguez, F., Célleri, R., and Peleg, N.: Are urban impacts on heavy rainfall amplified in mountainous regions?, Environmental Research Letters, 21, 044 016, https://iopscience.iop.org/article/10.1088/1748-9326/ae38f9, 2026.

Urgilés, G., Célleri, R., Bendix, J., and Orellana-Alvear, J.: Identification of spatio-temporal patterns in extreme rainfall events in the Tropical Andes: A clustering analysis approach, Meteorological Applications, 31, e70 005, https://doi.org/10.3390/rs13050991, 2024.

Viviroli, D., Dürr, H. H., Messerli, B., Meybeck, M., and Weingartner, R.: Mountains of the world, water towers for humanity: Typology, mapping, and global significance, Water resources research, 43, https://doi.org/10.1029/2006WR005653, 2007.

https://doi.org/10.5194/egusphere-2026-6670
Preprint. Discussion started: 4 November 2026
© Author(s) 2026. CC BY 4.0 License.



Wan, Z., Hook, S., and Hulley, G.: MODIS/Terra Land Surface Temperature/Emissivity Daily L3 Global 0.05Deg CMG V061, https://lpdaac.
775 usgs.gov/products/mod11c1v061/, accessed: 26 July 2026, 2021.

Wilks, D. S.: Statistical methods in the atmospheric sciences, vol. 100, Academic press, 2011.

Yoon, A., Hohenegger, C., Bao, J., and Brunner, L.: Extreme events in the Amazon after deforestation, Earth System Dynamics, 17, 167–179, https://doi.org/10.5194/esd-17-167-2026, 2026.